

# Performance study and conceptual design for the first implementation of AGATA at the in-flight RIB facility of GSI

C. Domingo-Pardo<sup>a,b</sup>, D. Bazzacco<sup>c</sup>, P. Doornenbal<sup>d</sup>, E. Farnea<sup>c</sup>, A. Gadea<sup>a</sup>, J. Gerl<sup>b</sup>, H.J. Wollersheim<sup>b</sup>  
The AGATA Collaboration

<sup>a</sup>*IFIC, CSIC-University of Valencia, Valencia, Spain*

<sup>b</sup>*GSI Helmholtzzentrum für Schwerionenforschung GmbH, Darmstadt, Germany*

<sup>c</sup>*Istituto Nazionale di Fisica Nucleare, Sezione di Padova, Italy*

<sup>d</sup>*RIKEN, Japan*

---

## Abstract

The main objective of the Advanced GAMMA Tracking Array (AGATA) is the investigation of the structure of exotic nuclei at the new generation of RIB facilities. As part of the preparatory phase for FAIR-NUSTAR, AGATA is going to be installed at the FRS fragmentation facility of the GSI center for an experimental campaign to be performed in 2012 and 2013. Owing to its  $\gamma$ -ray tracking capabilities and the envisaged enhancement in resolving power, a series of in-flight  $\gamma$ -ray spectroscopy experiments are being planned. The present work describes the conceptual design of this first implementation of AGATA at GSI-FRS, and provides information on the expected performance figures. According to the characteristics of each particular experiment, it is foreseen that the target-array distance is adjusted in order to achieve the optimum compromise between detection efficiency and energy resolution, or to cover an specific angular range of the emitted electromagnetic radiation. Thus, a comprehensive Monte Carlo study of the detection sensitivity in terms of photopeak efficiency, resolution and peak to total ratio, as a function of the target-array distance is presented. Several configurations have been investigated, and MC-calculations indicate that a remarkable enhancement in resolving power can be achieved when double-cluster AGATA detectors are developed and implemented. Several experimental effects are also investigated. This concerns the impact of passive materials between the target and the array, the angular distribution of the detection efficiency and the influence of target thickness effects and transition lifetimes in the attainable detection sensitivity. A short overview on halflife measurements via lineshape effects utilizing AGATA is also presented.

*Key words:* gamma-ray spectroscopy, tracking, Monte Carlo

---

## 1. Introduction

The study of nuclear structure far-off stability benefits from advances in both, acceleration techniques, as well as in detection systems. Since their invention in 1960, semiconductor germanium detectors represent key instruments in the field of high-resolution  $\gamma$ -ray spectroscopy. The unsurpassed energy resolution of germanium detectors has led to the discovery of new features and astounding properties of the atomic nucleus. Developments such as Ge-arrays like EUROBALL [1] and GAMMASPHERE [2] led to about two orders of magnitude improvement in resolving power when compared to the first generation of Compton-suppression arrays like HERA [3] or TESSA3 [4]. Remarkable results were, for example, the measurement of superdeformed nuclei with very high-angular-momentum states [5, 6, 7], thus revealing nuclear rotating systems with moments of inertia larger than  $80 \hbar^2 MeV^{-1}$ .

At present, the hot topics of nuclear structure with Radioactive Ion Beams (RIBs) concern the evolution of shell gaps and the related changes in magic numbers far-off stability; breakdown of isospin symmetry and its interplay with nuclear shape

evolution and shape coexistence phenomena; determination of the drip-line border of the nuclei chart and its link to open quantum systems, that in turn allow for understanding the coupling between bound states and the continuum; collectivity phenomena and electric and magnetic strength in nuclei, including also the investigation of giant resonances, as well as the fine structure in the Pygmy Dipole Resonance [9]. A deeper understanding of these scientific themes will become possible in the next future thanks to the combination of more exotic RIBs with state-of-the-art  $\gamma$ -ray detection systems. The latter concern the concept of  $\gamma$ -ray tracking. Owing to this novel approach, new generation arrays of 2D-segmented 3D-position sensitive detectors, such as the Advanced GAMMA Tracking Array (AGATA) in Europe [29] and the Gamma-Ray Energy Tracking Array (GRETA) in the USA [11] are being developed and early implementations are already used for in-beam  $\gamma$ -ray spectroscopy experiments.

Following a research and development phase including Monte-Carlo simulations and design studies [12, 13, 14, 15, 16, 17, 18], detector characterization [19, 20, 21, 22, 23, 24,

25, 26], technical developments [27, 28, 29], as well as a commissioning and in-beam test of the system [30, 31, 32, 33, 34, 35, 36, 37, 38] the first sub-array of AGATA, the so called AGATA Demonstrator, has been successfully set-up in operation at the stable ion beam facility of Laboratori Nazionali di Legnaro LNL-INFN (Italy) [? ].

In order to exploit best the complementarity offered by the different facilities in Europe, AGATA has been conceived as a peripatetic apparatus, which will itinerate from one facility to another. Thus, the next experimental campaign of the next AGATA construction phase will be carried out, during 2012 and 2013, at the GSI center for heavy ion research (Germany) in the framework of PreSPEC [39], which represents the preparatory phase for HISPEC/DESPEC at FAIR. HISPEC and DESPEC, which stand respectively for High-Resolution In-flight Spectroscopy and DEcay SPECTroscopy experiments, will be part of the NUSTAR (NUclear STructure, Astrophysics and Reactions) collaboration, the major next generation in-flight RIB facility in Europe. Similarly to the existing site at GSI, FAIR-NUSTAR will be based on the production of fragments from GeV/u beams and their separation in the Super-FRS [40]. The forthcoming stay of AGATA at GSI-FRS will benefit already from improvements in the beam intensities, which are a consequence of present accelerator developments towards FAIR. However, there are a number of relevant differences in the experimental conditions of GSI-FRS when compared to the previous host, INFN-LNL, which need to be taken into account. Such particularities concern mainly the relativistic momentum (typically  $\beta \sim 0.43$ ) and the spatial distribution ( $\text{FWHM}_x \sim 6$  cm) of the RIB at GSI-FRS, when compared to the narrow ( $\text{FWHM}_x \sim 2$  mm) stable beams, commonly used at INFN-LNL at lower velocities ( $\beta \lesssim 0.1$ ). Thus, in order to optimize its  $\gamma$ -ray efficiency and high intrinsic energy- and spatial-resolution, the configuration of the AGATA detectors needs to be designed according to the characteristics of the ion beam at the final focal plane of the GSI fragment separator (FRS). With this purpose, systematic Monte-Carlo (MC) simulations have been performed and their results are reported in this article. Sec. 2 summarizes the general features of the fragmentation facility at GSI, and the typical experimental conditions for in-flight  $\gamma$ -ray spectroscopy experiments using relativistic beams, with particular emphasis on the main differences in the experimental conditions with respect to the previous AGATA campaign, hosted at LNL-INFN.

MC-simulations reported in Sec. 3 illustrate the need of developing new double cluster detectors for an optimal use of AGATA with the RIBs available at GSI-FRS, as well as for the HISPEC experiment in the future FAIR-NUSTAR facility. Section 4 shows the attainable  $\gamma$ -ray detection sensitivity for such hybrid AGATA-shell geometries, with a variable number of double- and triple-cluster detectors. This seems convenient because of the non proportionality between efficiency and number of capsules. Also, results reported in that section should allow one to pick-up expected efficiency, resolution and peak to total (P/T) ratios, according to the number of crystals available for the array at the time of each particular experiment. The performance of several combinations of double- and triple-

cluster detectors, from 10 up to 40 capsules is displayed and tabulated. Photopeak efficiency, energy resolution and P/T ratios are represented as a function of the distance target-array, which can be adjusted for each particular experiment in order to find the best compromise according to the characteristics of the measurement.

The detection efficiency of AGATA varies with the  $\gamma$ -ray energy, which is also affected by the Lorentz boost. This dependency is reported in Sec. 5 for  $\gamma$ -quanta in the energy range from 500 keV up to 5 MeV and for several AGATA configurations. The Lorentz boost of the relativistic RIBs commonly used at GSI-FRS determines also, to a large extent, the angular distribution of the  $\gamma$ -ray detection efficiency. This relationship becomes of particular interest for a number of experiments (see e.g. [41]), as well as for the determination of reduced transition probabilities of excited states (see Sec. 9). Thus, Sec. 6 shows the angular variation of the photopeak efficiency for two AGATA configurations and for several target-array distances.

In the past campaigns with EUROBALL cluster detectors at GSI-FRS a thin shielding made of lead was commonly utilized for reducing atomic backgrounds. The impact of such additional passive materials on the detection efficiency of AGATA is presented in Sec. 7.

The impact of the half-life of the nuclear transition in combination with target thickness effects is reported in Sec. 8. A short overview on half-life measurement via lineshape effects is described in Sec. 9.

## 2. The GSI fragmentation facility and experimental conditions

The production of RIBs at the GSI-FRS facility starts with a high intensity stable beam delivered by the UNILAC linear accelerator, and accelerated to relativistic energies by the SIS18 synchrotron. This primary beam impinges on a target at a high energy, typically between 400 MeV/u and 1 GeV/u. This way, a broad spectrum of radioactive species is produced by means of fragmentation or induced fission reactions. The production target is in most cases a Be- or a Pb-layer with a thickness between 2 and 4 g/cm<sup>2</sup>. The fragments of interest are selected and transmitted through the fragment separator (FRS) using the  $B\rho$ - $\Delta E$ - $B\rho$  method. Details on the FRS can be found in Ref. [42]. The spatial profile of the fragments beam at the final focal plane of the FRS depends on several parameters, such as the beam energy and achromaticity. For energies of 100 MeV/u the beam shows a width of  $\lesssim 6$  cm FWHM in the dispersive horizontal plane  $X$  and about 4 cm FWHM on the vertical axis  $Y$  (see Fig. 1).

A secondary target, typically with a size of 62.5×62.5 mm<sup>2</sup>, is placed at the final FRS focal plane for inducing the reactions of interest in the impinging RIB. The target material is usually gold or lead for Coulomb excitation and beryllium for secondary fragmentation or particle knockout reactions. Thanks to the high secondary beam energy ( $\sim 100$  MeV/u) rather thick targets of 200 mg/cm<sup>2</sup> to 500 mg/cm<sup>2</sup> can be used, which allow one to enhance the reaction rate, while keeping the angular straggling of the reaction products within reasonable values of

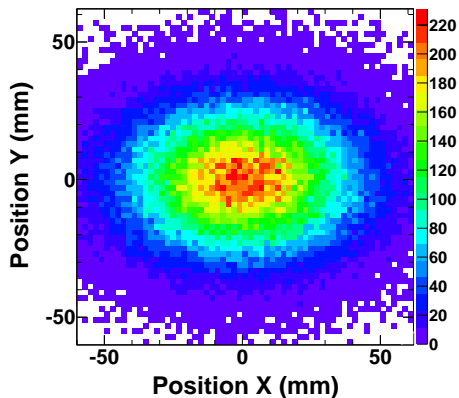


Figure 1: Transversal spatial distribution of the RIB at the final FRS focal plane for an energy of  $\sim 100$  MeV/u.

5-10 mrad. For many cases, such an enhancement on the reaction yield becomes of pivotal importance in order to access very exotic species, which are produced only in very small amounts. Because of the high ejectile velocity  $\beta$  the measured  $\gamma$ -ray energy  $E_\gamma$  appears shifted with respect to the  $\gamma$ -quantum energy at rest  $E_{\gamma,o}$ . This effect can be corrected by applying the Doppler formula,

$$E_{\gamma,o} = E_\gamma \frac{1 - \beta \cos \theta_\gamma}{\sqrt{1 - \beta^2}}, \quad (1)$$

where  $\theta_\gamma$  is the angle between the emitted  $\gamma$ -ray and the trajectory of the fragment in the laboratory frame. Thus, the accuracy with which the original  $\gamma$ -ray energy can be determined is defined by the uncertainty in the determination of the angle  $\theta_\gamma$  and the velocity  $\beta$  of the ion at the moment of  $\gamma$ -ray emission. In theory, three positions are needed in order to derive the value of the angle  $\theta_\gamma$ : the position of the ejectile both at de-excitation time and downstream from the target, and the location of the first  $\gamma$ -ray hit in AGATA. In practice, however, the ion position at de-excitation time can be measured only in an approximate way. Indeed, the two transversal  $(x, y)$  coordinates of the fragment are determined, approximately, utilizing a double-sided silicon-strip detector (DSSD) placed close to the secondary target. At present, there is no technique to measure the  $z$ -position of the reaction product at de-excitation time. For long half-lives such uncertainty dominates the width of the Doppler corrected  $\gamma$ -ray spectrum (see Sec. 8). The trajectory of the reaction products downstream from the target is made by means of the Lund-York-Cologne CALorimeter (LYCCA) [43], which also enables the measurement of the velocity of the fragments after the target  $\beta_{at}$ . Note that, in general, due to the energy loss in the target this quantity can be smaller than the velocity  $\beta$  at emission time, i.e.  $\beta_{at} \leq \beta$ , an effect which also has an impact in the attainable resolution (see Sec. 8). Finally, the 3D position sensitivity of AGATA, with an average FWHM  $\approx 4$  mm, provides the remaining information needed for the Doppler reconstruction of the  $\gamma$ -ray spectra. Further details about  $\gamma$ -ray spectroscopy

experiments with RIB at GSI-FRS using the RISING array of EUROBALL cluster detectors can be found in Ref. [44].

### 3. Reference case for the conceptual design The AGATA double cluster detectors

A simplified, although representative, physics case has been simulated in order to evaluate several possible geometrical detector configurations and determine the array design best suited for experiments at GSI-FRS. The figure of performance is based on the attainable  $\gamma$ -ray photopeak efficiency, peak to total (P/T) ratio and energy resolution. The MC-code used for this purpose is the one described in Ref. [15], with minor modifications in order to include the specific spatial  $x, y$ -profile of the RIB at the final focus of the FRS (see Fig. 1). Also the event generator of Ref. [15] was used to emit  $\gamma$ -rays with an energy at rest of  $E_{\gamma,o} = 1$  MeV emitted from a nucleus at a velocity of  $\beta = 0.43$ , equivalent to  $\sim 100$  MeV/u commonly used for Coulomb excitation and particle knockout experiments at GSI-FRS.

It is worth emphasizing that, for this conceptual design study, the effects of the target thickness and the half-life of the nuclear transition have been explicitly left aside. Such simplifications are convenient in order to tackle the problem in a systematic way. A negligible target thickness ensures no energy loss across the target, which implies a well defined velocity at de-excitation time ( $\beta = 0.43$ ). The impact of the target details, such as thickness and composition, in the Doppler reconstructed spectra is reported later in detail in Sec. 8. A negligible target thickness, in combination with a prompt de-excitation (half-life  $t_{1/2} = 0$ ) ensures also a well defined emission angle  $\theta_\gamma$ . The interplay between the value of the half-life and the target thickness is reported later in Sec. 9. These effects are expected to influence the performance of the array in the same direction for all configurations and therefore, such assumptions are not expected to affect the conclusions of this section.

Another simplification concerns the  $\gamma$ -ray multiplicity, which has been assumed to be  $M_\gamma = 1$  in all cases. Apart from the atomic background radiation,  $M_\gamma = 1$  is a reasonable assumption for both Coulomb excitation experiments  $M_\gamma^{Coulomb} = 1-2$  and particle knockout reactions  $M_\gamma^{Knockout} = 3-4$ .

In order to set-up a versatile  $\gamma$ -ray detection system with a limited number of capsules available, it is foreseen that the distance target-array is adjusted according to the characteristics of each particular experiment. Thus, large (short) target-array distances can be set-up in order to optimize detection resolution (efficiency). This feature is reasonable when the array consists of a relatively small amount of 30-40 capsules. A larger number of detectors covering a solid angle of  $2\pi$  or more would show approximately a constant variation of the efficiency with the target-array distance. An intermediate distance can be also chosen in order to settle a compromise between efficiency and resolution. The so-called “large” distance corresponds to 23.5 cm, which represents the center of the spherical shell defined by the front surface of the AGATA capsules. The “short” distance corresponds to a target-array distance of 8.5 cm. Thus, the evaluation of each configuration is based on MC simulations for

242 6 different target-array distances of 23.5, 18.5, 15.5, 13.5, 11.5  
 243 and 8.5 cm, each case containing  $5 \times 10^5$  events, which yields a  
 244 negligible statistical uncertainty for all quoted results.

245  $\gamma$ -Ray tracking has been implemented for the reconstruction  
 246 of the simulated events with the MGT-code [45]. MGT is used  
 247 with both packing and smearing distances equal to 5 mm and  
 248 intrinsic energy resolution for HPGe of 1.9 keV FWHM at  $E_\gamma =$   
 249 1.33 MeV with a noise component of 1 keV.

250 The first aspect to be considered for the installation of  
 251 AGATA at GSI is related to constraints arising from the size of  
 252 the RIB at the final focal plane of the FRS. Such statement also  
 253 holds concerning future implementations of AGATA for HIS-  
 254 PEC experiments at FAIR-NUSTAR. On one hand, as shown  
 255 in Fig. 1, because of the spatial spread of the RIB a beam-  
 256 pipe with a diameter of  $\gtrsim 80$  mm is required in order to avoid  
 257 excessive interactions of the outgoing reaction products with  
 258 the beam-pipe itself and another structural materials. Calcula-  
 259 tions of the ion-beam optics through the current design of the  
 260 Super-FRS [46] indicate that the size of the beam at its final  
 261 focal plane should be comparable to the one shown in Fig. 1.  
 262 On the other hand, the geometrical design of AGATA is done  
 263 aiming to maximize the solid angle coverage, thus reducing to  
 264 the minimum the size of the pentagonal holes [15]. The latter  
 265 turn out to be sufficiently large for the beam output at LNL-  
 266 INFN, but they are too small for the beam at GSI-FRS. The  
 267 most straightforward solution would consist of removing two of  
 268 the central triple clusters of the  $1\pi$  AGATA configuration, and  
 269 rotate slightly the array around the vertical axis, as it is shown  
 270 in Fig. 2-top. Nevertheless, this option shows two strong draw-  
 271 backs. First, it breaks the symmetry of the array, thus making  
 272 difficult the distribution of the detectors and leading to an irreg-  
 273 ular growth and solid angle coverage of the array. Second, the  
 274 irregular and relatively large insensitive area at forward angles  
 275 turn out to be the most relevant region in terms of efficiency  
 276 due to the effect of the Lorentz boost.

277 One possibility to improve this situation consists of develop-  
 278 ing and implementing double cluster detectors, which are built  
 279 of type B and C capsules. This way, the removal of the five  
 280 capsules of A type positioned around the pentagonal hole in the  
 281 beam axis is done by using an inner ring of five double cluster  
 282 detectors. Thus, this AGATA implementation will be an hybrid  
 283 configuration of double and triple cluster detectors, still in a  
 284  $1\pi$  symmetric AGATA setup (see Fig. 2-bottom). This geome-  
 285 try optimizes the large solid angle coverage at forward angles,  
 286 while leaving enough space for the RIB passing downstream  
 287 towards LYCCA. Such approach yields a remarkable enhance-  
 288 ment in performance when compared with any other possibility  
 289 based only on triple cluster detectors. This is shown in Fig. 3,  
 290 where the photopeak efficiency, energy resolution and P/T ratio  
 291 are displayed as a function of the distance between the sec-  
 292 ondary target and the AGATA array. In this case, the geome-  
 293 try based on triple clusters consists of 13 ATCs (39 capsules),  
 294 as shown in Fig. 2-top. The new hybrid geometry is based on  
 295 an outer ring of 10 ATCs, supplemented with an inner ring of  
 296 5 AGATA Double Cluster (ADC) detectors (40 capsules), as  
 297 shown in Fig. 2-bottom. Thus, an enhancement of up to 20%  
 298 in efficiency can be achieved, whereas the resolution and P/T

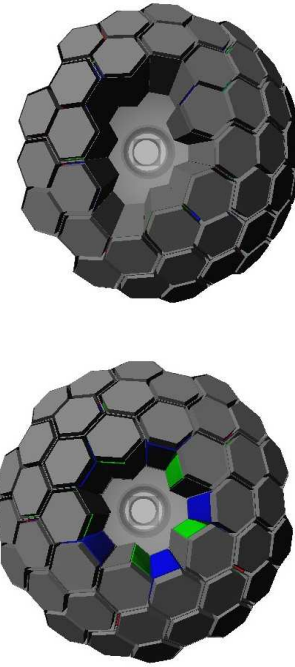


Figure 2: (Top) Shell geometry with 13 triple cluster detectors. (Bottom) Hybrid shell geometry with 5 double- and 10-triple cluster detectors.

ratios remain essentially the same. The tracking efficiency of MGT typically varies between 60% and 80% for short (8.5 cm) and large (23.5 cm) target-array distances, respectively.

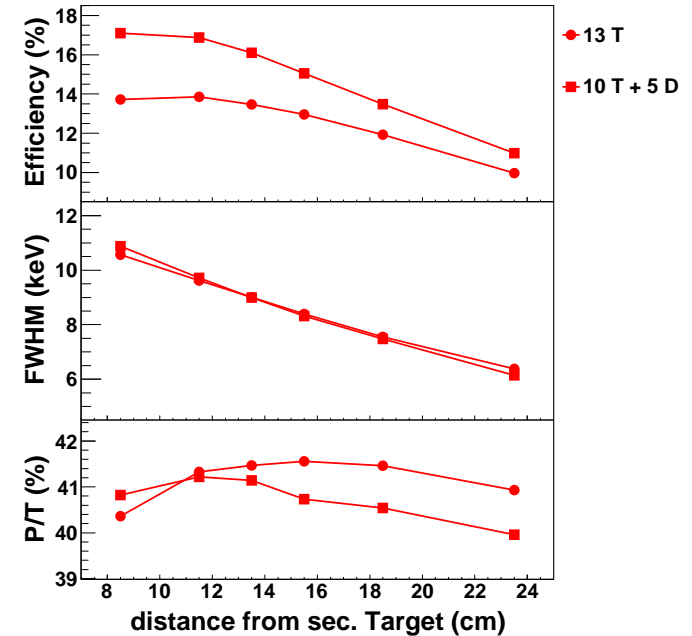


Figure 3: Photopeak efficiency (top) resolution (middle) and P/T ratio (bottom) for two AGATA configurations: 13 triple clusters (circles) shown in Fig. 2-top, and 5 double- plus 10 triple-cluster detectors (squares) shown in Fig. 2-bottom.

The increasing detection sensitivity with decreasing target-

303 array distances reflects both, the effect of the larger solid-angle  
 304 and the Lorentz boost at velocities of  $\beta \sim 0.43$ . The latter rep-  
 305 resents indeed an advantage in terms of detection efficiency, as  
 306 it is illustrated in the top panel of Fig. 4, where the performance  
 307 of the 10 T+5 D geometry is shown for a projectile velocity of  
 308  $\beta = 0.43$  and at rest  $\beta = 0$ .

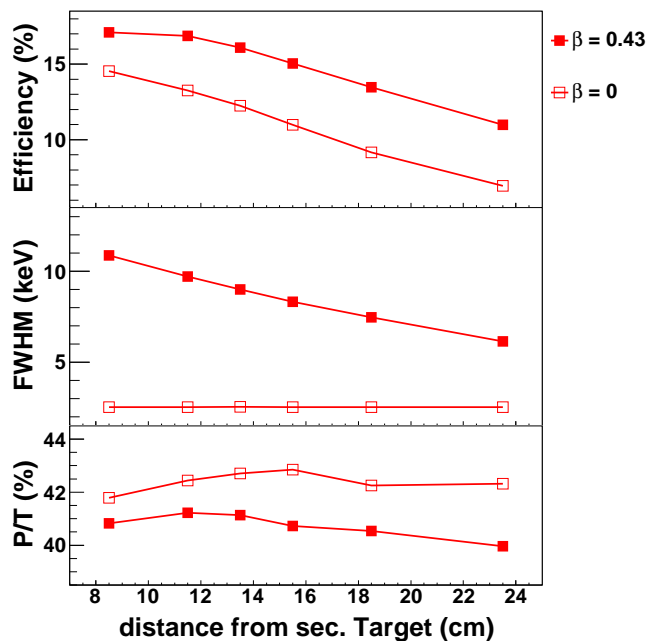


Figure 4: Photopeak efficiency (top) resolution (middle) and P/T ratio (bottom) for the 10 ATC + 5 ADC AGATA configuration, at relativistic projectile energy  $\beta = 0.43$  (solid symbols) and at rest  $\beta = 0$  (open symbols).

309 Another configurations thoroughly investigated were based  
 310 on compact cylindrical geometries, where the AGATA triple-  
 311 cluster detectors were separated from each other, and arranged  
 312 around the target chamber for maximizing the solid angle cover-  
 313 age. This approach had the disadvantage that  $\gamma$ -ray tracking  
 314 could be only applied within each triple-cluster detector, thus  
 315 reducing the overall performance of the array, and limiting no-  
 316 tably the scalability of the array on a long term basis.

317 In summary, the MC performance figures indicate that an hy-  
 318 brid shell-geometry, based on an inner ring of 5 double cluster  
 319 detectors, and an outer ring of triple cluster detectors (as many  
 320 as available) represents the best approach for nuclear structure  
 321 studies using relativistic RIBs at the GSI-FRS facility and at the  
 322 future FAIR-NUSTAR site.

#### 323 4. Performance of the hybrid shell geometry

324 The aforementioned non-scalability of the efficiency with the  
 325 number of capsules in the array, makes it worth quantifying the  
 326 performance of the hybrid array as a function of the number  
 327 of double- and triple-cluster detectors available. Using the ref-  
 328 erence case described in the section above, table 1 shows the  
 329 expected performance in terms of  $\gamma$ -ray photopeak efficiency,  
 330 resolution and P/T-ratio as a function of the number of triple

331 and double cluster detectors present in the setup and for sev-  
 332 eral secondary target to array distances. For the sake of clarity,  
 333 these values are shown in Fig. 5 only for configurations consist-  
 334 ing of  $n$  triple- and 5 double-cluster detectors ( $n$  T+5 D),  
 335 with  $n$  from 0 up to 10 triple clusters. Fig. 6 shows the perfor-  
 336 mance for 5 ATC and a variable number of ADCs (5 T+ $n$  D),  
 337 with  $n$  from 0 up to 5 double cluster detectors. In the latter  
 338 figure, also the combination 0 T+5 D is shown. It is worth em-  
 339 phasizing the similarity in performance between the 0 T+5 D  
 340 and the 5 T+0 D cases (see solid circles and open squares in  
 341 Fig. 6), which illustrates, once more, the relevance of devel-  
 342 oping AGATA double cluster detectors for experiments at GSI.  
 343 Indeed, 10 capsules arranged in a ring of 5 ADCs, show already  
 344 the same performance as 15 capsules arranged in a half-ring of  
 345 5 ATC detectors. In this respect, it is also important to remark  
 346 the non-linear dependence of the detection efficiency on the  
 347 number of capsules, as a consequence of  $\gamma$ -ray tracking. For  
 348 example, the 5 T+0 D case corresponds to an intrinsic photo-  
 349 peak efficiency of 0.13% per capsule. On the other hand, the  
 350 5 T+5 D configuration shows an efficiency of 0.22% per cap-  
 351 sule, which indicates a relative enhancement of the detection  
 352 efficiency per capsule of 66%.

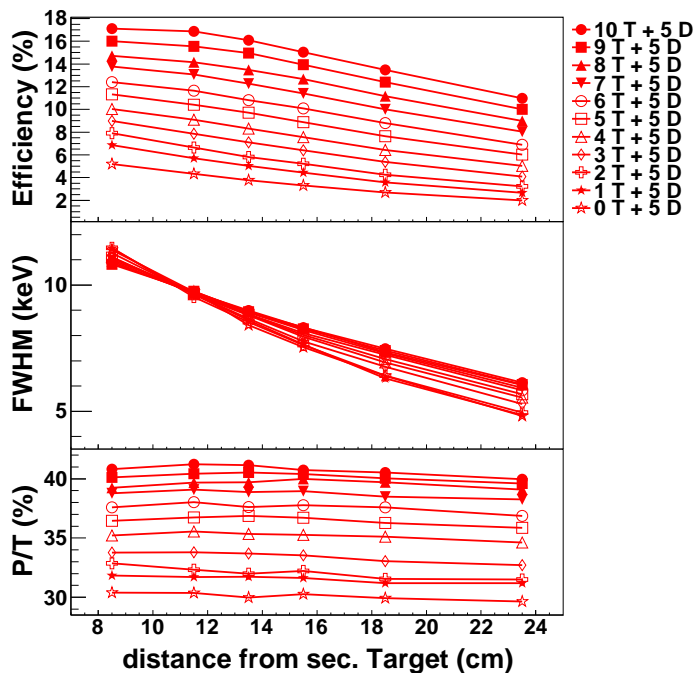


Figure 5: Reference case. Efficiency (top), resolution (middle) and P/T ratio (bottom) as a function of the number of triple (#T) cluster detectors in the setup. The number of double cluster detectors is always 5.

353 For the first experiments with AGATA at GSI, it is expected  
 354 that at least 5 ATC and 5 ADC are available. Therefore, for  
 355 nuclear transitions of 1 MeV emitted at  $\beta = 0.43$ , photopeak  
 356 efficiencies in the range of 6 to 11% and energy resolutions of  
 357 6 to 11 keV should be attainable (depending on the distance  
 358 target array) with a P/T ratio of about 36%. Depending on the  
 359 rate of detector delivery and acceptance, it is expected to in-  
 360 crease gradually the number of ATCs. This should allow one

Table 1: Performance of the AGATA array as a function of the number of double and triple AGATA cluster detectors. For each configuration indicated in the left-hand side of the table, the three rows represent the efficiency, resolution and P/T ratio, respectively.

# T	# D	distance target-array (cm)						
		23.5	18.5	15.5	13.5	11.5	8.5	
10	5	11.0	13.5	15.1	16.1	16.9	17.1	$\epsilon_\gamma$ (%)
		6.1	7.5	8.3	9.0	9.7	10.9	FWHM (keV)
		40.0	40.5	40.7	41.1	41.2	40.8	P/T (%)
9	5	10.0	12.4	13.9	14.9	15.6	16.0	$\epsilon_\gamma$ (%)
		6.1	7.4	8.3	8.9	9.7	10.8	FWHM (keV)
		39.6	40.0	40.4	40.5	40.4	40.1	P/T (%)
8	5	9.0	11.2	12.7	13.5	14.1	14.7	$\epsilon_\gamma$ (%)
		6.0	7.3	8.3	8.9	9.7	10.9	FWHM (keV)
		39.1	39.7	40.0	39.7	39.7	39.2	P/T (%)
7	5	8.0	10.0	11.4	12.3	13.1	13.8	$\epsilon_\gamma$ (%)
		5.9	7.3	8.2	8.9	9.8	11.0	FWHM (keV)
		38.3	38.5	39.0	38.9	39.1	38.8	P/T (%)
6	5	6.9	8.8	10.1	10.8	11.6	12.4	$\epsilon_\gamma$ (%)
		5.8	7.2	8.1	8.8	9.7	11.1	FWHM (keV)
		36.9	37.6	37.8	37.6	38.0	37.6	P/T (%)
5	5	6.0	7.6	8.9	9.7	10.4	11.3	$\epsilon_\gamma$ (%)
		5.7	7.1	8.0	8.8	9.7	11.1	FWHM (keV)
		35.8	36.3	36.7	36.9	36.7	36.5	P/T (%)
4	5	5.0	6.4	7.6	8.3	9.1	10.0	$\epsilon_\gamma$ (%)
		5.5	6.9	7.9	8.8	9.6	11.1	FWHM (keV) <sup>361</sup>
		34.6	35.1	35.3	35.3	35.5	35.2	P/T (%) <sup>362</sup>
3	5	4.1	5.4	6.4	7.1	7.9	9.0	$\epsilon_\gamma$ (%) <sup>363</sup>
		5.3	6.8	7.8	8.7	9.6	11.3	FWHM (keV) <sup>364</sup>
		32.7	33.0	33.5	33.7	33.8	33.8	P/T (%) <sup>365</sup>
2	5	3.2	4.2	5.2	5.8	6.7	7.9	$\epsilon_\gamma$ (%) <sup>366</sup>
		4.9	6.4	7.6	8.5	9.5	11.5	FWHM (keV) <sup>367</sup>
		31.5	31.5	32.2	32.0	32.3	32.9	P/T (%) <sup>368</sup>
1	5	2.7	3.6	4.4	5.0	5.7	6.8	$\epsilon_\gamma$ (%) <sup>369</sup>
		4.9	6.3	7.6	8.6	9.6	11.4	FWHM (keV) <sup>370</sup>
		31.2	31.2	31.6	31.7	31.7	31.8	P/T (%) <sup>371</sup>
0	5	2.0	2.7	3.3	3.8	4.3	5.2	$\epsilon_\gamma$ (%) <sup>372</sup>
		4.8	6.4	7.5	8.4	9.7	11.4	FWHM (keV) <sup>373</sup>
		29.6	29.9	30.3	30.0	30.4	30.4	P/T (%) <sup>374</sup>
5	4	5.1	6.5	7.6	8.3	9.0	10.1	$\epsilon_\gamma$ (%)
		5.6	6.9	8.0	8.8	9.7	11.3	FWHM (keV)
		34.7	35.1	35.5	35.4	35.3	35.3	P/T (%) <sup>374</sup>
5	3	4.1	5.3	6.3	7.1	7.8	9.0	$\epsilon_\gamma$ (%)
		5.3	6.7	7.8	8.7	9.6	11.2	FWHM (keV) <sup>375</sup>
		32.4	33.0	33.4	33.5	33.5	33.8	P/T (%) <sup>376</sup>
5	2	3.2	4.3	5.2	5.9	6.6	7.9	$\epsilon_\gamma$ (%) <sup>377</sup>
		4.9	6.4	7.7	8.5	9.7	11.4	FWHM (keV) <sup>378</sup>
		31.1	31.6	32.3	32.3	32.5	32.7	P/T (%) <sup>379</sup>
5	1	2.6	3.6	4.4	5.1	5.7	6.8	$\epsilon_\gamma$ (%) <sup>380</sup>
		4.8	6.2	7.5	8.5	9.5	11.5	FWHM (keV) <sup>381</sup>
		30.9	30.9	31.7	31.9	31.5	32.1	P/T (%) <sup>382</sup>
5	0	2.0	2.7	3.3	3.8	4.3	5.1	$\epsilon_\gamma$ (%) <sup>383</sup>
		4.7	6.3	7.6	8.4	9.5	11.6	FWHM (keV) <sup>384</sup>
		29.7	30.0	30.2	30.2	30.2	30.2	P/T (%) <sup>385</sup>

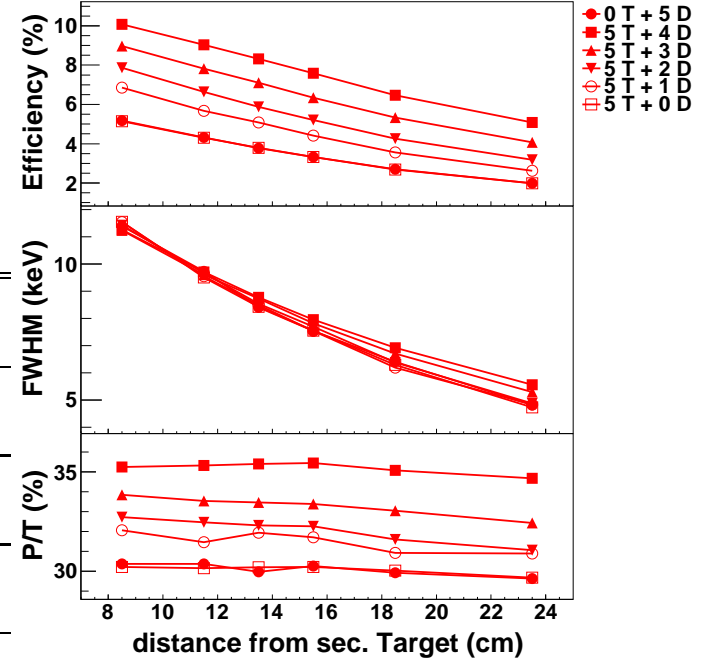


Figure 6: Reference case. Efficiency (top), resolution (middle) and P/T ratio (bottom) as a function of the number of double (#D) AGATA cluster detectors in the setup. All configurations comprise 5 ATC.

to enhance the aforementioned values up to 11-17% photopeak efficiency, 6-11 keV FWHM energy resolution and  $\sim 40\%$  P/T-ratio. It is worth noting that, at least in terms of efficiency, there is an optimal target-array distance. However, the latter depends on the number and type of cluster detectors available. Thus, for a relatively small amount of clusters, there is a substantial enhancement in the efficiency when going from 11.5 cm to 8.5 cm, e.g.  $\sim 9\%$  enhancement for 5 T+5 D. However, such variation is of only 1% for the 10 T+5 D configuration.

The chosen  $\gamma$ -ray energy of  $E_{\gamma,0} = 1$  MeV corresponds only to an average representative value, which is close to many experiments of interest for nuclear structure. Values for another  $\gamma$ -ray energies are reported below in Sec. 5.

## 5. Dependence of the performance on the $\gamma$ -ray energy

The complex dependency of the detection efficiency on the  $\gamma$ -ray transition energy using relativistic RIBs requires a MC simulation study. On one hand, the Lorentz boost concentrates a large amount of  $\gamma$ -quanta in the forward direction, thus enhancing the detection probability for small values of the angle  $\theta_\gamma$ , mostly in the region covered by the double cluster detectors. But on the other hand, this effect is counterbalanced to some extent by the Doppler shift in energy, which increases the  $\gamma$ -ray energy at the same forward angles, thus reducing the detection efficiency correspondingly. In order to quantify the impact of these effects in the performance of the tracking array, MC simulated values for efficiency, resolution and P/T-ratio, are tabulated and displayed in this section for a range of  $\gamma$ -ray energies from 500 keV up to 5 MeV. Results are displayed reported

<sup>386</sup>

<sup>387</sup>

<sup>388</sup>

389 for three reference hybrid-shell AGATA geometries, namely  
 390 10 ATC+5 ADC (Fig. 7, Table 2), 7 ATC+5 ADC (Fig. 8, Ta-  
 391 ble 3) and 5 ATC+5 ADC (Fig. 9, Table 4).

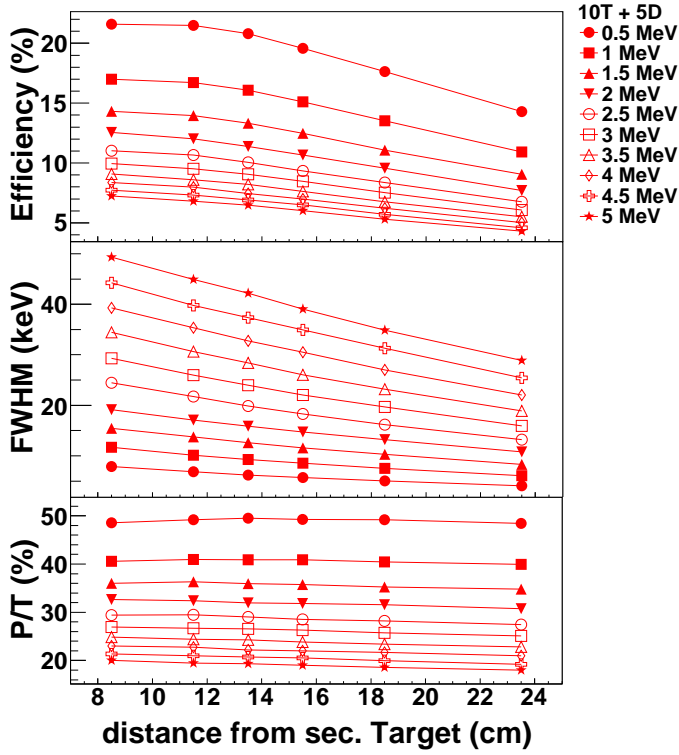


Figure 7: Photopeak efficiency (top), resolution (middle) and P/T ratio (bottom) for 10 triple + 5 double AGATA cluster detectors. Each curve corresponds to one  $\gamma$ -ray energy (see label). In all cases  $\beta = 0.43$ .

Table 2: 10 triple + 5 double AGATA configuration, efficiency and energy resolution values as a function of the  $\gamma$ -ray energy at rest  $E_{\gamma,o}$  and  $\beta = 0.43$ .

$E_{\gamma,o}$ (MeV)	distance target-array (cm)						
	23.5	18.5	15.5	13.5	11.5	8.5	
0.5 MeV	14.3	17.6	19.6	20.8	21.5	21.6	$\epsilon_\gamma$ (%)
	4.1	5.0	5.7	6.2	6.9	7.9	FWHM (keV)
	48.4	49.2	49.2	49.5	49.2	48.6	P/T (%)
1 MeV	10.9	13.5	15.1	16.1	16.7	17.0	$\epsilon_\gamma$ (%)
	6.1	7.5	8.5	9.3	10.1	11.7	FWHM (keV)
	39.9	40.5	40.9	40.9	41.0	40.6	P/T (%)
1.5 MeV	9.1	11.1	12.5	13.3	14.0	14.3	$\epsilon_\gamma$ (%)
	8.3	10.3	11.6	12.6	13.8	15.4	FWHM (keV)
	34.8	35.2	35.7	35.9	36.3	36.0	P/T (%)
2 MeV	7.7	9.6	10.7	11.4	12.0	12.6	$\epsilon_\gamma$ (%)
	10.8	13.2	14.7	15.9	17.1	19.1	FWHM (keV)
	30.8	31.5	31.8	31.9	32.4	32.6	P/T (%)
2.5 MeV	6.8	8.4	9.3	10.1	10.7	11.0	$\epsilon_\gamma$ (%)
	13.2	16.2	18.3	19.9	21.7	24.5	FWHM (keV)
	27.4	28.2	28.5	29.0	29.5	29.4	P/T (%)
3 MeV	6.1	7.5	8.5	9.1	9.5	9.9	$\epsilon_\gamma$ (%)
	15.9	19.7	22.0	24.0	26.0	29.3	FWHM (keV)
	25.1	25.7	26.3	26.6	26.7	26.9	P/T (%)
3.5 MeV	5.5	6.8	7.6	8.2	8.6	9.1	$\epsilon_\gamma$ (%)
	18.9	23.2	26.0	28.4	30.6	34.4	FWHM (keV)
	22.8	23.4	23.9	24.3	24.4	24.8	P/T (%)
4 MeV	5.0	6.2	7.0	7.5	8.0	8.4	$\epsilon_\gamma$ (%)
	22.0	27.0	30.5	32.8	35.3	39.3	FWHM (keV)
	21.0	21.7	22.0	22.2	22.8	23.0	P/T (%)
4.5 MeV	4.6	5.7	6.5	6.9	7.3	7.7	$\epsilon_\gamma$ (%)
	25.4	31.3	34.9	37.3	39.8	44.2	FWHM (keV)
	19.2	20.0	20.5	20.7	21.0	21.4	P/T (%)
5 MeV	4.3	5.3	6.0	6.5	6.8	7.2	$\epsilon_\gamma$ (%)
	28.9	34.9	39.0	42.2	44.9	49.3	FWHM (keV)
	18.0	18.6	19.0	19.3	19.5	20.0	P/T (%)

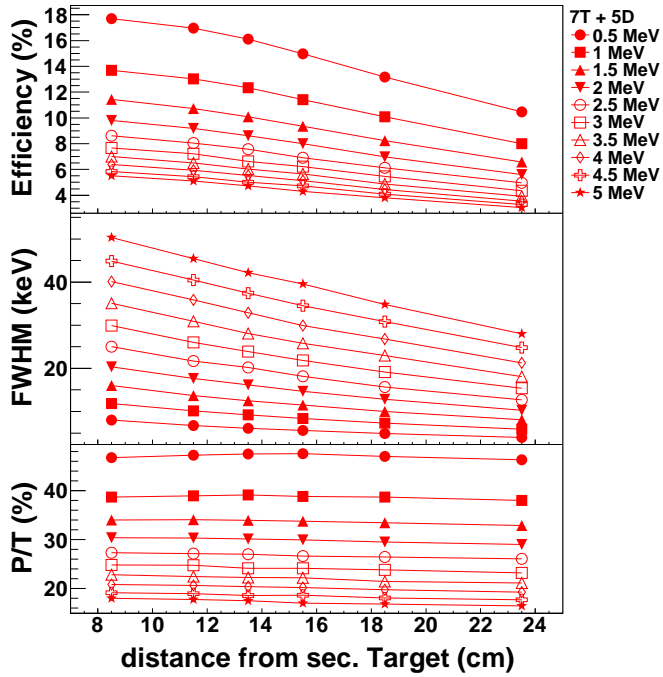


Figure 8: Photoppeak efficiency (top), resolution (middle) and P/T ratio (bottom) for 7 triple + 5 double AGATA cluster detectors. Each curve corresponds to one  $\gamma$ -ray energy (see figure label). In all cases  $\beta = 0.43$ .

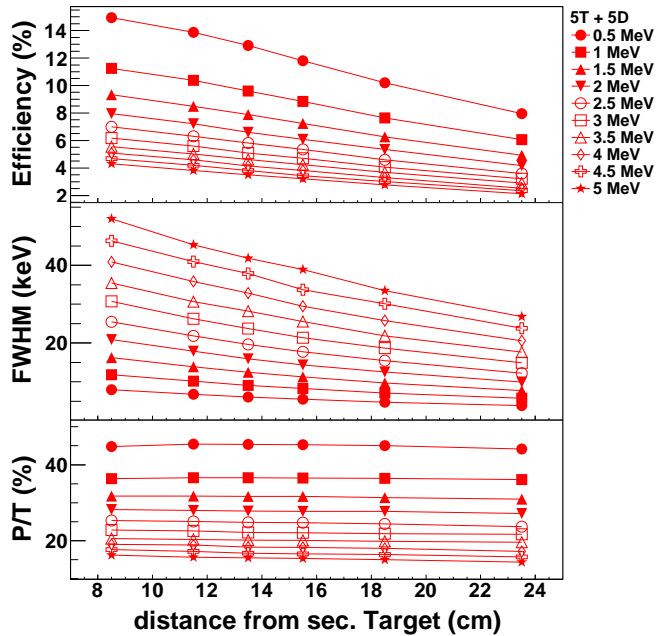


Figure 9: Photoppeak efficiency (top), resolution (middle) and P/T ratio (bottom) for 5 triple + 5 double AGATA cluster detectors. Each curve corresponds to one  $\gamma$ -ray energy (see figure label). In all cases  $\beta = 0.43$ .

Table 3: 7 triple + 5 double AGATA configuration, efficiency, energy resolution and P/T-ratio values as a function of the  $\gamma$ -ray energy at rest  $E_{\gamma,o}$  and  $\beta = 0.43$ .

$E_{\gamma,o}$ (MeV)	distance target-array (cm)						
	23.5	18.5	15.5	13.5	11.5	8.5	
0.5 MeV	10.5	13.2	15.0	16.1	17.0	17.7	$\epsilon_\gamma$ (%)
	3.9	4.9	5.6	6.1	6.8	8.0	FWHM (keV)
	46.3	47.0	47.6	47.5	47.2	46.7	P/T (%)
1 MeV	8.0	10.1	11.4	12.3	13.0	13.7	$\epsilon_\gamma$ (%)
	5.9	7.3	8.4	9.2	10.1	11.8	FWHM (keV)
	38.0	38.7	38.8	39.1	38.9	38.7	P/T (%)
1.5 MeV	6.6	8.2	9.4	10.1	10.7	11.4	$\epsilon_\gamma$ (%)
	8.1	10.0	11.5	12.5	13.7	16.0	FWHM (keV)
	32.9	33.4	33.8	33.9	34.0	34.0	P/T (%)
2 MeV	5.6	7.0	8.0	8.6	9.2	9.8	$\epsilon_\gamma$ (%)
	10.3	12.8	14.7	16.1	17.7	20.3	FWHM (keV)
	29.0	29.5	29.9	30.1	30.3	30.4	P/T (%)
2.5 MeV	5.0	6.1	6.9	7.6	8.0	8.6	$\epsilon_\gamma$ (%)
	12.7	15.7	18.2	20.2	21.7	25.0	FWHM (keV)
	26.1	26.5	26.6	27.0	27.1	27.3	P/T (%)
3 MeV	4.3	5.4	6.2	6.6	7.2	7.7	$\epsilon_\gamma$ (%)
	15.4	19.2	21.9	23.9	26.0	30.0	FWHM (keV)
	23.2	23.8	24.2	24.1	24.8	24.8	P/T (%)
3.5 MeV	3.9	4.9	5.7	6.0	6.5	7.0	$\epsilon_\gamma$ (%)
	18.1	22.9	25.8	28.1	30.9	35.1	FWHM (keV)
	21.2	21.5	22.2	22.3	22.5	22.8	P/T (%)
4 MeV	3.5	4.4	5.1	5.5	5.9	6.4	$\epsilon_\gamma$ (%)
	21.3	26.8	29.9	32.9	35.9	40.1	FWHM (keV)
	19.2	19.8	20.2	20.4	20.7	20.9	P/T (%)
4.5 MeV	3.3	4.1	4.7	5.0	5.4	5.8	$\epsilon_\gamma$ (%)
	24.8	30.8	34.6	37.4	40.5	44.9	FWHM (keV)
	17.7	18.1	18.6	18.6	19.0	19.2	P/T (%)
5 MeV	3.0	3.8	4.3	4.7	5.1	5.5	$\epsilon_\gamma$ (%)
	28.0	34.8	39.5	42.2	45.4	50.3	FWHM (keV)
	16.4	16.8	17.0	17.5	17.8	18.0	P/T (%)

Table 4: 5 triple + 5 double AGATA configuration, efficiency and resolution values as a function of the  $\gamma$ -ray energy at rest  $E_{\gamma,o}$  and  $\beta = 0.43$ .

$E_{\gamma,o}$ (MeV)	distance target-array (cm)						
	23.5	18.5	15.5	13.5	11.5	8.5	
0.5 MeV	8.0	10.2	11.8	12.9	13.9	14.9	$\varepsilon_\gamma$ (%)
	3.8	4.7	5.5	6.0	6.8	8.0	FWHM (keV)
	44.1	45.0	45.2	45.4	45.4	44.8	P/T (%)
1 MeV	6.1	7.6	8.8	9.6	10.4	11.2	$\varepsilon_\gamma$ (%)
	5.7	7.1	8.2	9.1	10.2	11.8	FWHM (keV)
	36.1	36.4	36.5	36.6	36.6	36.4	P/T (%)
1.5 MeV	4.9	6.3	7.2	7.9	8.5	9.3	$\varepsilon_\gamma$ (%)
	7.7	9.7	11.3	12.4	13.8	16.2	FWHM (keV)
	30.9	31.4	31.7	31.7	31.7	31.8	P/T (%)
2 MeV	4.2	5.4	6.1	6.6	7.2	8.0	$\varepsilon_\gamma$ (%)
	9.9	12.5	14.3	15.9	17.9	20.8	FWHM (keV)
	27.2	27.8	27.7	27.8	28.0	28.2	P/T (%)
2.5 MeV	3.6	4.6	5.4	5.8	6.3	7.0	$\varepsilon_\gamma$ (%)
	12.2	15.4	17.7	19.6	21.8	25.4	FWHM (keV)
	23.7	24.4	24.8	24.8	25.0	25.3	P/T (%)
3 MeV	3.2	4.1	4.7	5.1	5.6	6.2	$\varepsilon_\gamma$ (%)
	14.9	18.7	21.4	23.7	26.2	30.7	FWHM (keV)
	21.7	21.8	22.1	22.1	22.6	22.8	P/T (%)
3.5 MeV	2.9	3.7	4.2	4.6	5.0	5.6	$\varepsilon_\gamma$ (%)
	17.7	21.8	25.5	28.2	30.6	35.5	FWHM (keV)
	19.6	19.8	20.1	20.2	20.3	20.6	P/T (%)
4 MeV	2.5	3.3	3.8	4.2	4.6	5.1	$\varepsilon_\gamma$ (%)
	20.5	25.8	29.4	32.9	35.9	40.9	FWHM (keV)
	17.2	18.0	18.2	18.3	18.8	19.0	P/T (%)
4.5 MeV	2.3	3.0	3.5	3.8	4.2	4.7	$\varepsilon_\gamma$ (%)
	23.8	30.1	33.7	37.9	41.0	46.3	FWHM (keV)
	15.7	16.4	16.5	16.7	17.2	17.6	P/T (%)
5 MeV	2.1	2.8	3.2	3.5	3.8	4.3	$\varepsilon_\gamma$ (%)
	26.8	33.5	38.9	41.8	45.3	51.9	FWHM (keV)
	14.4	15.0	15.3	15.5	15.7	16.2	P/T (%)

Angular distribution measurements of  $\gamma$ -rays emitted by oriented nuclei have been a fundamental tool to investigate their multipolarity and electromagnetic character (see e.g. Ref. [47]). In addition, the angular distribution of the prompt  $\gamma$ -rays emitted after Coulomb excitation allows one to distinguish between the electromagnetic and the nuclear contributions to the excited states. Such studies were performed in the past using an array of EUROBALL cluster detectors [48, 41]. The high granularity of AGATA in conjunction with the large angular range represent a substantial advantage in order to study angular distributions in detail. The broad angular coverage arises not only from the number of germanium crystals available, but also from the possibility to shift the secondary target downstream by 15 cm. This is illustrated in Figure 10, where the  $\gamma$ -ray efficiency for  $E_{\gamma,o} = 1$  MeV emitted from a nucleus at  $\beta = 0.43$  is displayed as a function of the angle  $\theta_\gamma$  in intervals of  $\Delta\theta_\gamma = \pm 5^\circ$ .

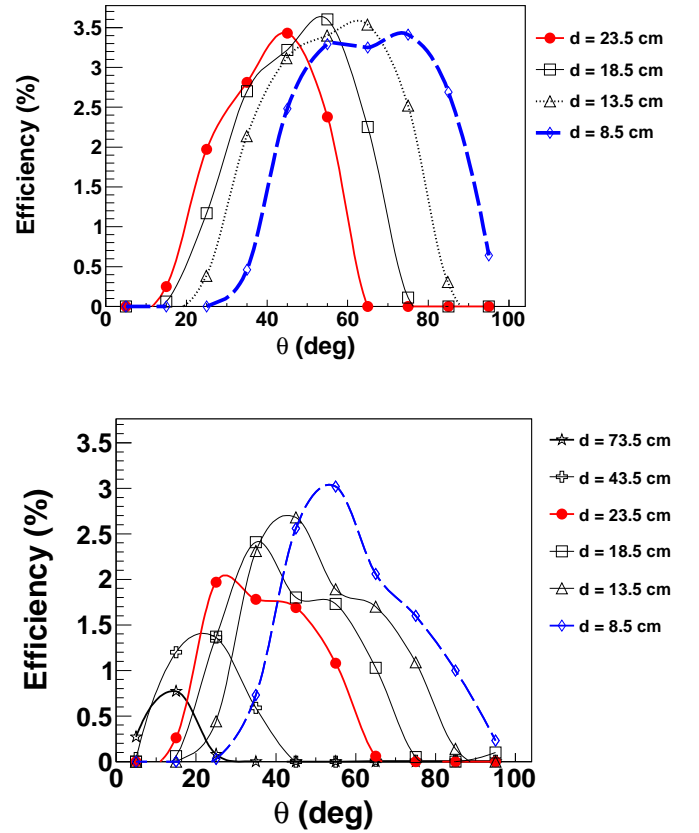


Figure 10: Efficiency as a function of the  $\gamma$ -ray detection angle  $\theta_\gamma$  for  $E_{\gamma,o} = 1$  MeV emitted at  $\beta = 0.43$ . (Top) A simulation with 10 triple and 5 double AGATA cluster detectors, (bottom) 5 triple and 5 double clusters [73.5 cm and 43.5 cm distributions to be removed in bottom figure].

Thus, in the AGATA configuration of 10 triple and 5 double cluster detectors, angles between  $15^\circ$  and  $90^\circ$  can be covered with angular efficiencies larger than 1% over  $\Delta\theta = 10^\circ$ . Note that at relativistic beam energies ( $\beta \sim 0.43$ ), the largest differences between the electromagnetic and the nuclear interactions are obtained at  $\theta_\gamma \simeq 25^\circ$  and at  $\theta_\gamma \simeq 60^\circ$ . At these an-

gles, the proposed geometry allows one to achieve efficiencies of more than 2.5% over an interval of  $\Delta\theta_\gamma = \pm 5^\circ$ .

The angular distribution of the first interaction reflects the contribution in efficiency of both, the inner ring of double-cluster and the outer ring of triple-cluster detectors, even if they are not independent. These two contributions are most visible in the “short” distance configuration ( $d=8.5$  cm), where two maxima can be observed at  $\sim 55^\circ$  and at  $\sim 75^\circ$  (see Fig.10 top). Comparing the angular distribution of 10 T+5 D (Fig. 10 top) against that of 5 T+5 D (Fig. 10 bottom), one can indeed observe a reduction in the efficiency due to the lowering of the second maximum, i.e. the contribution of the outer ring of only five triple cluster detectors.

## 7. Impact of passive materials

At the final stage of the GSI-FRS the main source of  $\gamma$ -ray background is due to the slowing-down of ions and light-charged particles, flying through layers of materials such as the energy-degrader, the secondary target, the tracking detectors and other structural materials like the beam-pipe and holding structures. Experimental  $\gamma$ -ray spectra with such a background are shown in previous publications [41, 49]. A description of this background at the lower beam-energies used in decay spectroscopy experiments is reported in Ref. [50]. In order to suppress effectively this contaminant bremsstrahlung’s radiation a lead layer of 2 mm thickness was installed around the EUROBALL cluster detectors in the past campaigns. In a similar way, it might be convenient to put a lead shielding around the reaction chamber to reduce the background in AGATA. This is a possibility which will be investigated during the commissioning of AGATA at GSI. The effect of such a lead layer with different thicknesses around the target chamber to shield the AGATA detectors is illustrated in Fig. 11, which shows the result of a MC simulation for  $E_{\gamma,o} = 1$  MeV emitted at  $\beta = 0.43$ . Three configurations have been considered in the simulation, *i*) 10 triple + 5 double, *ii*) 5 triple + 5 double and *iii*) 5 double cluster detectors. Indeed, the impact of a lead layer, both in the efficiency and in the P/T ratio, becomes larger for the ATCs than for the ADCs, and also for the short target-array distance of 8.5 cm than for the nominal distance (see Fig. 11). This reflects the energy shift due to the large Doppler effect at relativistic velocities, which yields smaller energies (larger absorption) at the larger angles subtended by the ATCs, when compared to the small angles (larger energy) subtended by the ADCs. The resolution (not shown in Fig. 11) remains practically unaffected.

[Add a similar figure for another g-ray energies: e.g. 500 keV and 2 MeV (?).]

## 8. Interplay between target thickness and half-life of the nuclear transition

The impact of the target characteristics and the excited state lifetime on the shape of Doppler corrected  $\gamma$ -ray spectra has been thoroughly investigated in Ref. [51] for in-beam  $\gamma$ -ray experiments at relativistic energies using the RISING array. A similar study for AGATA is presented in this section.

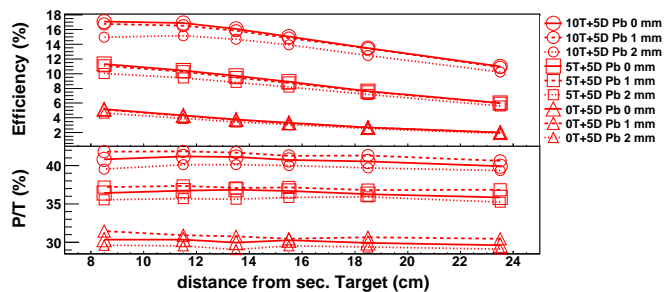


Figure 11: Biggest symbols represent values without lead absorber, the empty symbols with decreasing size show the deterioration of the efficiency (top panel) and P/T ratio (bottom) due to a layer of lead in-front of the detectors. See legend for proper interpretation of the absorber thickness. MC simulation performed for  $E_{\gamma,o} = 1$  MeV emitted at  $\beta = 0.43$ .

The convoluted effect of the excited state lifetime and the energy loss across the target thickness is due to the fact that the target is a passive element and therefore, both the ejectile velocity and position at de-excitation time, in general, remain unknown. In practice, only the measurement of the ejectile velocity after the target,  $\beta_{at}$ , becomes feasible. If the lifetime is sufficiently short, so that the average de-excitation path is shorter than the target thickness, most of the transitions still occur inside the target, where no kinematics information is available, i.e. the velocity at de-excitation time  $\beta$  is different, larger, than the velocity measured after the target  $\beta_{at}$  with LYCCA (see Sec. 2). On the other hand, nuclei with relatively long half-lives de-excite predominantly beyond the secondary target, and the velocity at de-excitation time  $\beta$  coincides with the velocity measured after the target  $\beta_{at}$ . In the latter case the Doppler correction becomes precise in terms of velocity. However, the position downstream along the beam axis  $z$  at de-excitation time remains still unknown and the true  $\gamma$ -ray emission angle  $\theta_\gamma$  is larger than the one commonly assumed, which corresponds to de-excitations at the center of the target. This feature introduces an exponential tail towards low energy in the Doppler corrected photopeak, which is larger the longer is the lifetime. In general, the shape of the Doppler reconstructed spectrum reflects the contribution of these two effects, whose relative influence depends sensitively on the beam and target characteristics, as well as on the precise value of the transition lifetime. In order to illustrate this, a series of MC simulations have been carried out, with an AGATA configuration consisting of 10 ATC and 5 ADC, with secondary targets of Au and Be, with thicknesses of 250 and 500 mg/cm<sup>2</sup> and target-array distances of 8.5 and 23.5 cm. These are the most extreme scenarios in terms of optimizing detection efficiency, resolution or reaction yield (see Sec. 2 and Sec. 3). For each case, transition half-lives between 0 ps and 100 ps have been simulated.

The physics case corresponds to a medium-heavy nucleus ( $Z=29$ ,  $A=75$ ) impinging at a velocity of  $\beta = 0.43$  in the secondary target, and undergoing a one-proton knockout reaction. The spatial distribution along the beam direction  $z$  assumed for the generation of the primary events in the simulation corresponds to a constant excitation cross section across the path of the nucleus through the target. The event generator is the

509 one described in Ref. [51] with only minor updates to interface  
 510 with the standard AGATA-code [15]. A transition energy of  
 511  $E_{\gamma,o} = 1$  MeV is assumed in all cases.

### 512 8.1. Light secondary target

513 The Doppler corrected spectra for beryllium targets of 250  
 514 and 500 mg/cm<sup>2</sup> are shown in Fig. 12 and Fig. 13, respectively.  
 515 Also the spectrum corresponding to an ideally thin target is  
 516 shown in those figures for comparison.

517 For the Doppler correction the (measurable) ejectile velocity  
 518 after the target,  $\beta_{at}$ , has been considered and the  $\gamma$ -ray emission  
 519 angle in the laboratory system,  $\theta_\gamma$ , has been calculated assum-  
 520 ing a de-excitation position along the beam axis at  $z = 0$  cm,  
 i.e., at the center of the target. The width of the photopeak

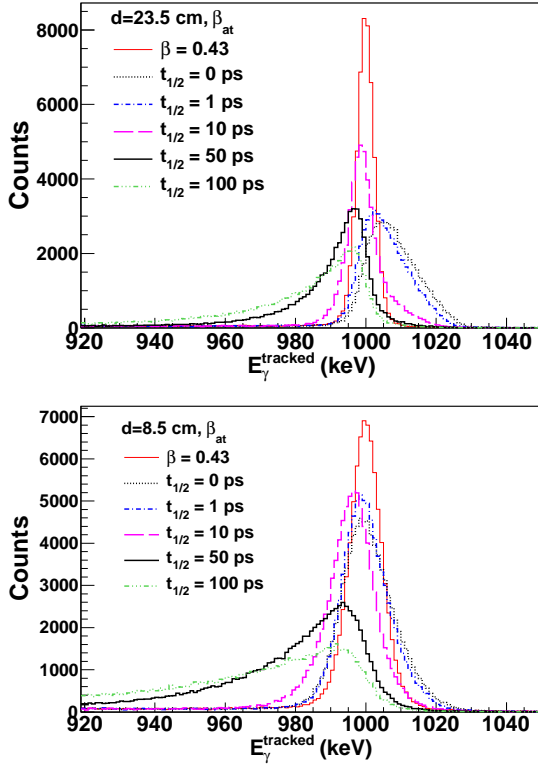


Figure 12: Effect of the lifetime and the energy loss across a 250 mg/cm<sup>2</sup> thick beryllium target. The velocity after the target has been taken for the Doppler reconstruction. Simulation for target-array distance of 23.5 cm (top) and 8.5 cm (bottom). The thin-solid line (labeled as  $\beta = 0.43$ ) corresponds to an ideal target of negligible thickness and prompt de-excitations ( $t_{1/2} = 0$  ps). See text for details.

521 reconstructed via MGT is reported in table 5. Note that in some  
 522 cases the shape of the reconstructed photo-peak is rather asym-  
 523 metric, and in those situations the value of the FWHM is not very  
 524 representative.

525 As it was mentioned before, the main deviations from the  
 526 ideal target case arise from two experimental effects. On one  
 527 hand, for transitions where  $t_{1/2}$  is small the width of the re-  
 528 constructed peak is dominated by energy loss effects inside the  
 529 target and the corresponding uncertainty on  $\beta$  at de-excitation  
 530 time. As shown in the top panel of Fig.13, this effect is par-  
 531 ticularly prominent for the 500 mg/cm<sup>2</sup> target and for half-lives  
 532

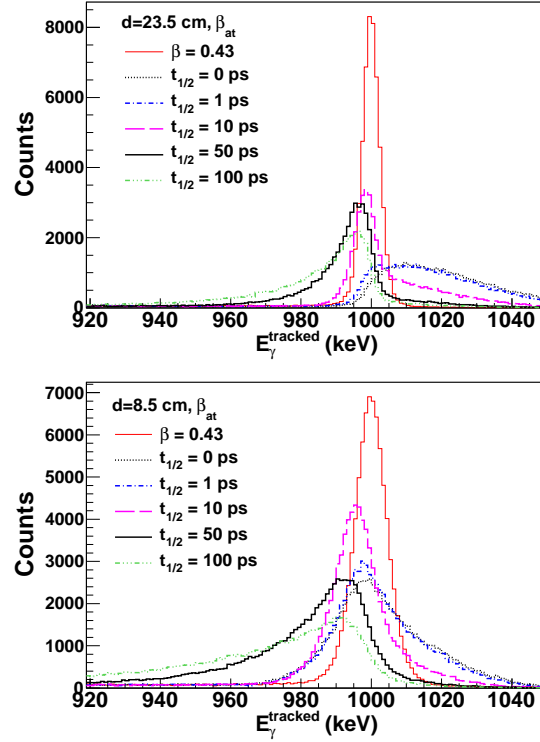


Figure 13: Same as Fig.12, but for a 500 mg/cm<sup>2</sup> thick Be-target.

Table 5: Energy resolution for a beryllium target and for several assumptions on the thickness and the half-life of the transition.

$t_{1/2}$ (ps)	RESOLUTION FWHM (keV)			
	250 mg/cm <sup>2</sup>		500 mg/cm <sup>2</sup>	
	d=23.5 cm	d=8.5 cm	d=23.5 cm	d=8.5 cm
0	16.8	18.6	33.1	~32
1	15.9	16.7	35.5	27.2
10	11.2	16.9	9.2	16.5
50	16.8	~35	14.8	19.5
100	~30	~50	18.2	~30

533  $t_{1/2} \lesssim 1$  ps. The tail towards high  $\gamma$ -ray energy is due to the  
 534 assumption  $\beta \sim \beta_{at}$ . Actually, the fact that  $\beta > \beta_{at}$  introduces a  
 535 shift in the value of the Doppler reconstructed energy towards  
 536 high energy (see Eq. 1). On the other hand, for transitions with  
 537 large halfives ( $t_{1/2} \gtrsim 50$  ps) the width of the reconstructed peak  
 538 is dominated by the uncertainty on the de-excitation position  $z$   
 539 along the beam axis. Assuming a de-excitation at  $z = 0$  leads  
 540 to an emission angle  $\theta_\gamma$  smaller than the true angle downstream  
 541  $z > 0$ , an effect which goes in the opposite direction than the  
 542 aforementioned  $\beta \sim \beta_{at}$  approximation, shifting the value of the  
 543 reconstructed energy towards low energy.

544 A remarkable improvement in the width of the reconstructed  
 545 photopeak can be obtained if the value of the transition halfife  
 546 is known, particularly for transitions with short lifetimes. In-  
 547 deed, in these cases one can calculate the mean value for both,  
 548 the ejectile velocity and the  $z$ -position at de-excitation time, and  
 549 use them for the Doppler correction. In order to illustrate this  
 550 we choose the example of the 500 mg/cm<sup>2</sup> Be-target at 8.5 cm<sup>576</sup>  
 551 (see Fig. 13-bottom). Table 6 shows the mean values of  $\beta$  and  $z$ <sup>577</sup>  
 552 at de-excitation time obtained from the MC-simulation.<sup>578</sup>

580 Table 6: Mean  $\beta$  and  $z$  values at de-excitation time for the 500 mg/cm<sup>2</sup> thick  
 581 Be-target.

$\tau$ (ps)	$\langle \beta \rangle$	$\langle z \rangle$ (mm)
0	0.401	0.0
1	0.397	0.2
10	0.380	1.8
50	0.371	8.8
100	0.369	17.5

553 As shown in Fig. 14, when instead of  $\beta_{at}$  and  $z = 0$ , the mean  
 554 values of table 6 are used for the Doppler correction, one ob-  
 555 tains rather symmetric distributions (at least for  $t_{1/2} < 50$  ps), as  
 556 well as an improvement in the width of the Doppler corrected  
 557 photopeak ( $\lesssim 20$  keV FWHM for all transitions with  $t_{1/2} < 50$  ps).  
 558 On the other hand, when the value of the halfife is unknown,  
 559 one can apply a multiple Doppler correction, assuming differ-  
 560 ent values for the lifetime, and implementing in each case the  
 561 corresponding mean position and velocity values. This might  
 562 lead to an improved Doppler corrected spectrum, as well as to  
 563 an estimate of the transition lifetime. More precise methods for  
 564 the measurement of the lifetime are reported in Sec. 9.

## 565 8.2. Heavy secondary target

566 For secondary samples made of gold, the intrinsic stopping  
 567 power is higher than for beryllium, but the distance which the  
 568 ejectile needs to travel in order to cross the sample is a factor  
 569 of 10 smaller. For gold targets one obtains the spectra shown  
 570 in Fig. 15 and in Fig.16, for thicknesses of 250 mg/cm<sup>2</sup> and<sup>582</sup>  
 571 500 mg/cm<sup>2</sup>, respectively. The values for the energy resolu-<sup>583</sup>  
 572 tion are listed in Table 7. For halfives between 1 ps and 10 ps,<sup>584</sup>  
 573 for both target thicknesses most of the decays happen already<sup>585</sup>  
 574 after the target, thus yielding in both cases a rather thin distribu-<sup>586</sup>  
 575 tion, which is only 1-4 keV broader than the ideally thin targets<sup>587</sup>

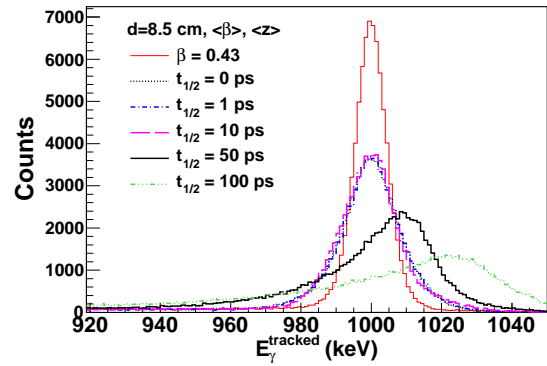


Figure 14: Same as Fig. 13-bottom, but assuming that the transition halfife is known, which allows one to use the mean velocity  $\langle \beta \rangle$  and the mean position  $\langle z \rangle$  values at de-excitation time for the Doppler correction of the spectrum.

case. This applies for both distances target-array of 23.5 cm and 8.5 cm. For shorter ( $t_{1/2} < 1$  ps) or larger ( $t_{1/2} > 10$  ps) halfives, the width of the reconstructed peak increases by a factor of two, or more, owing to the aforementioned effects of larger uncertainties on  $\beta$  and on  $z$ -position at de-excitation time, respectively.

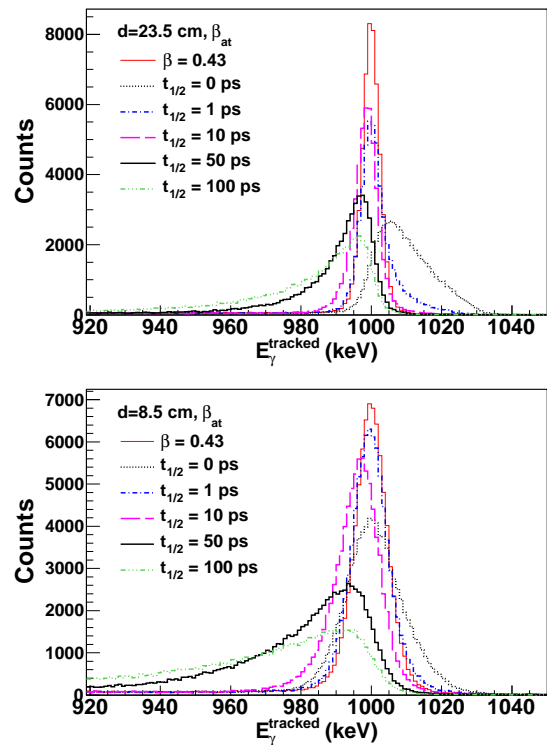


Figure 15: Same as Fig. 12, but for a gold target with a thickness of 250 mg/cm<sup>2</sup>.

In summary, the attainable resolution at 1 MeV ranges between 7 keV and  $\gtrsim 20$  keV. The precise value depends sensitively on the projectile kinematics and characteristics (its atomic and mass numbers), target thickness and material, the target-array distance and the lifetime of the expected nuclear transition. In this respect, for the successful plan of in-flight

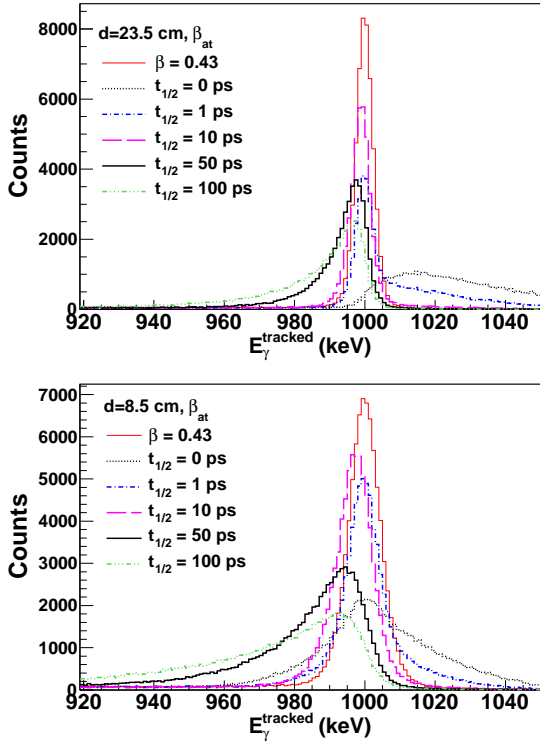


Figure 16: Same as Fig. 15, but for a gold target with a thickness of 500 mg/cm<sup>2</sup>.

Table 7: Energy resolution for a gold target and for several assumptions on the thickness and the half-life of the transition.

$t_{1/2}$ (ps)	RESOLUTION FWHM (keV)			
	250 mg/cm <sup>2</sup>		500 mg/cm <sup>2</sup>	
	d=23.5 cm	d=8.5 cm	d=23.5 cm	d=8.5 cm
0	16.4	19.9	~39	~34
1	8.9	13.4	6.9	15.3
10	8.4	15.2	7.1	13.4
50	14.4	14.4	11.7	18.2
100	~28	~33	12.5	26.5

588 experiments at GSI-FRS, it becomes convenient to perform in  
 589 advance dedicated MC simulations, which include all these in-  
 590 gredients in a realistic way. This should allow one to optimize  
 591 the experimental setup, and also select the secondary ion beam  
 592 and the kinematics, which are best suited for the aim of each  
 593 particular measurement.

## 594 9. Lifetime measurement

595 As described in Ref. [51], there are essentially two effects  
 596 that can be exploited in order to evaluate the effective transition  
 597 lifetime from the shape of the corresponding peak. The first one  
 598 makes use of the dependence of the emission point along the  
 599 beam axis  $z$  with the transition half-life. The second one uses  
 600 the emission during the slow-down process. In this case the  
 601 asymmetry of the reconstructed peak is larger at small angles.

602 The high position resolution, together with the possibility to  
 603 work at target-array distance of 8.5 to 23.5 cm, makes AGATA  
 604 particularly well suited for both methods.

### 605 9.1. Large lifetimes via centroid-shift at large angles

606 As described above in Sec. 8, this effect arises from the de-  
 607 pendence of the average distance from reaction to de-excitation  
 608 on the value of the lifetime. Whereas for short lifetimes  
 609 ( $t_{1/2} \lesssim 1$  ps) the excited nucleus de-excites inside the target and,  
 610 in good approximation, the mean de-excitation position along  
 611 the beam axis corresponds to  $z \sim 0$ , for large lifetimes ( $\sim 100$  ps)  
 612 this value is shifted towards higher distances  $z \sim \text{cm}$ , thus be-  
 613 ing the real emission angle larger than the one obtained from  
 614 the  $z = 0$  assumption used for the Doppler reconstruction, and  
 615 shifting the centroid of the  $\gamma$ -ray peak towards lower energy.  
 616 Since the velocity of the products at  $\beta \sim 0.4$  is of the order of  
 617 0.1-0.2 mm/ps, this effect is more evident for lifetime values of  
 618 few tens to hundreds of ps. The best angular range to exploit  
 619 this effect corresponds to angles, such that  $\cos(\theta_\gamma) = \beta$  [51].  
 620 Thus, for the typical relativistic beam velocities of GSI-FRS  
 621  $\beta = 0.43$ ,  $\theta_\gamma \sim 65^\circ$  and, as shown in Fig. 10, the optimal  
 622 AGATA configurations for covering such angles are those for  
 623 target-array distances of 8.5 cm to 13.5 cm. The peak centroid-  
 624 shift effects e.g. for a 250 mg/cm<sup>2</sup> Be target at 8.5 cm become  
 625 evident in the spectra shown in the bottom panel of Fig. 12.  
 626 The systematics of this shift with the half-life are displayed in  
 627 Fig. 17, which demonstrates that half-lives in the range of 10 ps  
 628 to 100 ps can be inferred via this method.

629 Because of the subtended angle and the range of half-lives,  
 630 the shape of these spectra (Fig. 12-bottom) is dominated by the  
 631 centroid-shift ( $z > 0$ ) effects, although a small component to-  
 632 wards high energy can be still appreciated for short half-lives  
 633  $t_{1/2} \lesssim 1$  ps. The high angular resolution of AGATA can be  
 634 utilized here in order to disentangle the  $z > 0$  effect of inter-  
 635 est (which shifts the peak centroid towards lower values), from  
 636 the effects of de-excitation during deceleration (which shift the  
 637 distribution towards high energy). Thus, by applying an angu-  
 638 lar cut at  $64^\circ < \theta_\gamma < 66^\circ$ , one obtains the distributions shown  
 639 in Fig. 18, which are fully dominated by the  $z > 0$  effect.

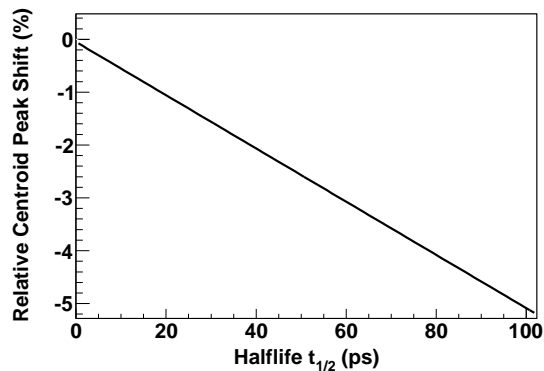


Figure 17: Systematics of the peak centroid shift for a 250 mg/cm<sup>2</sup> Be-target at 8.5 cm from the array (see text for details).

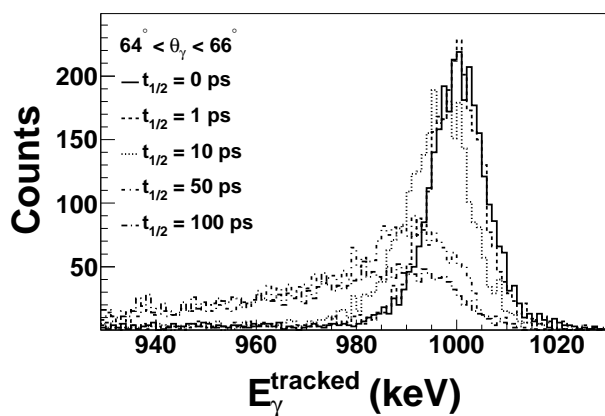


Figure 18: Line shape reconstructed for the 250 mg/cm<sup>2</sup> Be-target at 8.5 cm applying an angular cut of  $65 \pm 1^\circ$ .

## 9.2. Small lifetimes via Doppler Shift Attenuation Method

For lifetimes of few ps the Doppler-reconstructed photopeak typically shows two components. One of them is centered at the proper energy  $E_{\gamma,o}$ , and arises from de-excitations happening shortly after the target, where the velocity remains constant and can be measured. The second contribution extends towards  $E_\gamma > E_{\gamma,o}$ , and is due to de-excitations inside the target, where  $\beta > \beta_{at}$ . This tail towards high energy becomes more prominent at small angles (see Eq. 1). Indeed, at small angles  $\theta_\gamma$  the shape of the Doppler corrected spectrum reflects the shape of the velocity distribution at de-excitation time. Fig. 19 shows quantitatively this effect for the example described in Sec. 8, now assuming half-life values between 0.25 ps and 1.5 ps, a gold target of 500 mg/cm<sup>2</sup> and a secondary beam energy of 150 MeV/u. Fig. 20 shows the Doppler reconstructed peak for several angu-

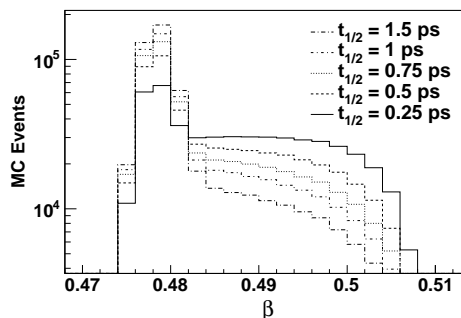


Figure 19:  $\beta$ -value at de-excitation time of the ejectile in a gold target 500 mg/cm<sup>2</sup> thick for an initial beam energy of 150 MeV/u.

lar slices of  $\Delta\theta_\gamma = 4^\circ$  at forward angles of the  $d = 23.5$  cm AGATA configuration, between  $22^\circ$  and  $42^\circ$ .

Thus, the fine angular resolution of AGATA allows one to measure accurately the angular evolution of the Doppler corrected photopeak. By comparing the systematics of this trend, versus detailed MC-simulations one can determine the value of rather fast nuclear transitions, approximately between 200 fs and 2 ps.

## 10. Summary and conclusions

The R&D and the final conceptual design of AGATA for experiments at GSI-FRS has been presented. The solution proposed requires the development of AGATA double cluster detectors, thus aiming at a full optimization of the tracking array for in-beam  $\gamma$ -ray spectroscopy experiments at this facility. A systematic study based on Monte Carlo simulations is reported, which comprises several parameters such as the distance target-array, number of detectors available, energy of the  $\gamma$ -ray transition and influence of passive elements. Thus, for relativistic beams with  $\beta = 0.43$ , using an AGATA configuration of 5 double- and 5 triple-cluster detectors, photopeak efficiencies between 6% and 11% can be obtained for  $E_{\gamma,o} = 1$  MeV (energy at rest), and target-array distances of 23.5 cm and 8.5 cm, respectively. These values become 11% and 17% respectively, when five additional triple cluster detectors would be available.

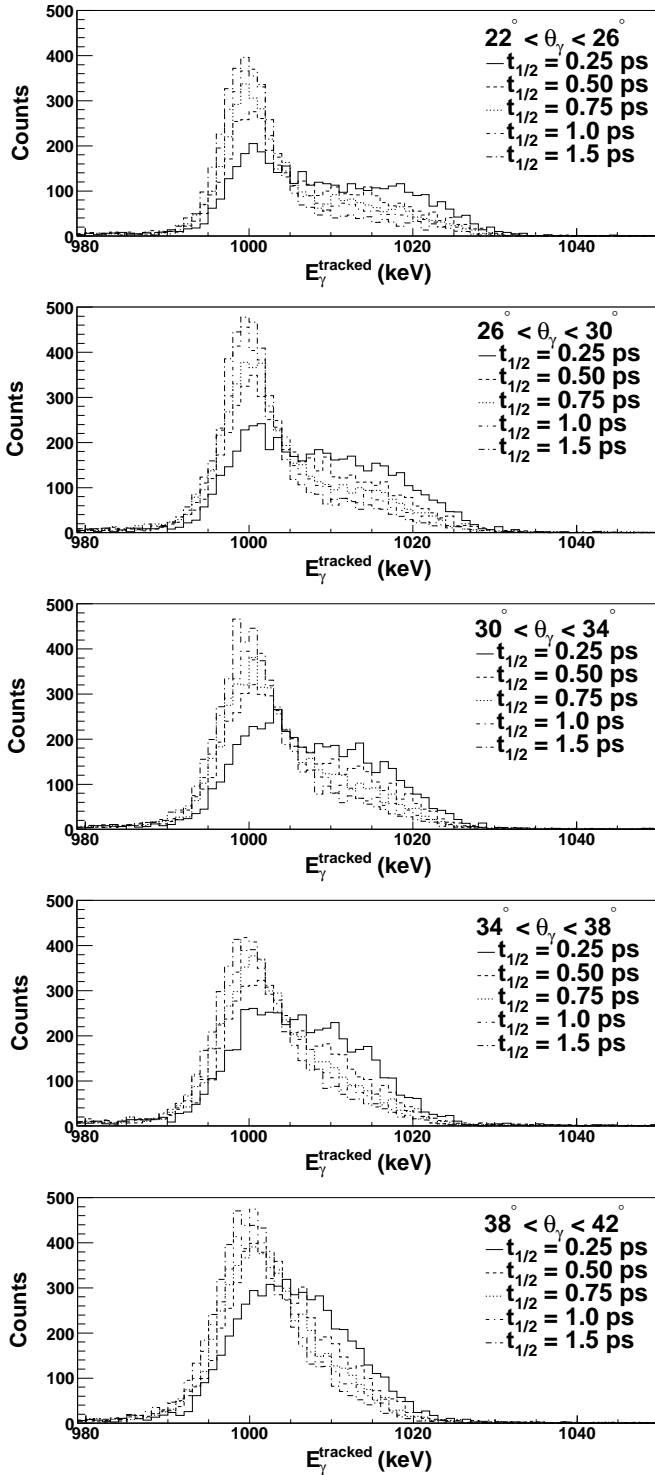


Figure 20: Doppler reconstructed spectra for several angular slices. Half-lives between 0.25 and 1.5 ps have been simulated. See text for details.

679 The energy resolution attainable in Doppler corrected spectra  
 680 depends on the particular experiment details and it seems to  
 681 be, in most cases, dominated by energy loss effects in the sec-  
 682 ondary target and by the half-life of the expected transition. In  
 683 this respect, it is recommended to carry out dedicated simula-  
 684 tions in order to obtain realistic values for each particular exper-  
 685 iment. As follow-up of a previous publication [51], the appli-  
 686 cation of lineshape effects measurable with AGATA for the de-  
 687 termination of transition half-lives has been investigated. Thus,  
 688 using the AGATA response at large angles  $\theta \sim 65^\circ$ , and at short  
 689 angles  $\theta \sim 20 - 30^\circ$ , our simulation shows that it is possible  
 690 to determine the value of half-lives of 10-100 ps, and 0.1-1 ps,  
 691 respectively.

## 692 Acknowledgement

693 The authors acknowledge support from HIC4FAIR. This  
 694 work has been supported in part by MEC (Spain) under grants  
 695 FPAXXX and FPAXXX.

## 696 References

- 697 [1] F. A. Beck. EUROBALL: Large gamma ray spectrometers through euro-  
 698 pean collaborations. *Progress in Particle and Nuclear Physics*, 28:443–  
 699 461, 1992.
- 700 [2] I. Y. Lee. The Gammasphere. *Nuclear Physics A*, 520:641–+, December  
 701 1990.
- 702 [3] R. M. Diamond, editor. *High-spin gamma-ray spectroscopy*, March 1984.
- 703 [4] P. J. Twin, P. J. Nolan, R. Aryaeinejad, D. J. G. Love, A. H. Nelson, and  
 704 A. Kirwan. TESSA : A multi-detector  $\gamma$ -ray array designed to study high  
 705 spin states. *Nuclear Physics A*, 409:343–351, November 1983.
- 706 [5] O. Moller, A. Dewald, P. Petkov, B. Saha, A. Fitzler, K. Jessen, D. Tonev,  
 707 T. Klug, S. Heinze, J. Jolie, P. von Brentano, D. Bazzacco, C. A.  
 708 Ur, E. Farnea, M. Axiotis, S. Lunardi, G. de Angelis, D. R. Napoli,  
 709 N. Marginean, T. Martinez, M. A. Caprio, and R. F. Casten. Electro-  
 710 magnetic transition strengths in  $^{156}\text{dy}$ . *Phys.Rev. C*, 74:024313, 2006.
- 711 [6] P. Petkov, A. Dewald, O. Moller, B. Saha, A. Fitzler, K. Jessen, D. Tonev,  
 712 T. Klug, S. Heinze, J. Jolie, P. von Brentano, D. Bazzacco, C. Ur,  
 713 E. Farnea, M. Axiotis, S. Lunardi, C. Rossi-Alvarez, G. de Angelis, D. R.  
 714 Napoli, N. Marginean, T. Martinez, M. Caprio, and R. F. Casten. Collec-  
 715 tivity at high spins in  $^{156}\text{dy}$ . *Phys.Rev. C*, 68:034328, 2003.
- 716 [7] M. A. Caprio, N. V. Zamfir, R. F. Casten, C. J. Barton, C. W. Beau-  
 717 sang, J. R. Cooper, A. A. Hecht, R. Krucken, H. Newman, J. R. Novak,  
 718 N. Pietralla, A. Wolf, and K. E. Zyranski. Low-spin structure of  $^{156}\text{dy}$   
 719 through  $\gamma$ -ray spectroscopy. *Phys.Rev. C*, 66:054310, 2002.
- 720 [8] P. J. Twin, B. M. Nyakó, A. H. Nelson, J. Simpson, M. A. Bentley, H. W.  
 721 Cranmer-Gordon, P. D. Forsyth, D. Howe, A. R. Mokhtar, J. D. Morrison,  
 722 J. F. Sharpey-Schafer, and G. Sletten. Observation of a discrete-line su-  
 723 perdeformed band up to  $60\hbar$  in  $^{152}\text{Dy}$ . *Physical Review Letters*, 57:811–  
 724 814, August 1986.
- 725 [9] Perspectives of Nuclear Physics in Europe, NuPECC Long Range Plan  
 726 2010, 2010. European Science Foundation.
- 727 [10] J. Gerl, W. Korten (Eds.), AGATA: Technical Proposal for an Advanced  
 728 Gamma Tracking Array for the European Gamma Spectroscopy Commu-  
 729 nity, (2001) <<http://agata.pd.infn.it>>.
- 730 [11] M. A. Deleplanque, I. Y. Lee, K. Vetter, G. J. Schmid, F. S. Stephens,  
 731 R. M. Clark, R. M. Diamond, P. Fallon, and A. O. Macchiavelli. GRETA:  
 732 utilizing new concepts in  $\gamma$ -ray detection. *Nuclear Instruments and Meth-  
 733 ods in Physics Research A*, 430:292–310, July 1999.
- 734 [12] F. Camera. AGATA: The European HPGe tracking array. In A. J. Kreiner  
 735 & O. Civitarese, editor, *VI Latin American Symposium on Nuclear  
 736 Physics and Applications*, volume 884 of *American Institute of Physics  
 737 Conference Series*, pages 97–102, February 2007.
- 738 [13] E. Ince, E. Farnea, A. Latina, and M. N. Erduran. Realistic simulations  
 739 of the AGATA Demonstrator+PRISMA Spectrometer. In I. Boztosun &

- 740 A. B. Balantekin, editor, *American Institute of Physics Conference Series*,<sup>811</sup>  
741 volume 1072 of *American Institute of Physics Conference Series*, pages<sup>812</sup>  
742 273–276, November 2008.
- 743 [14] E. Farnea. The AGATA Demonstrator Array at Laboratori Nazionali di<sup>814</sup>  
744 Legnaro: Status of the Project. In M. Milin, T. Niksic, S. Szilner, &<sup>815</sup>  
745 D. Vretenar, editor, *American Institute of Physics Conference Series*, vol-<sup>816</sup>  
746 ume 1165 of *American Institute of Physics Conference Series*, pages 390–<sup>817</sup>  
747 393, August 2009.
- 748 [15] The Agata Collaboration, E. Farnea, F. Recchia, D. Bazzacco, T. Kröll,<sup>819</sup>  
749 Z. Podolyák, B. Quintana, A. Gadea, and The AGATA Collaboration.<sup>820</sup>  
750 Conceptual design and Monte Carlo simulations of the AGATA array.<sup>821</sup>  
751 *Nuclear Instruments and Methods in Physics Research A*, 621:331–343,<sup>822</sup>  
752 September 2010.
- 753 [16] The Agata, Prisma Collaborations, E. Ince, M. N. Erduran, E. Farnea,<sup>824</sup>  
754 A. Latina, G. Pollarolo, and The AGATA and PRISMA Collaborations.<sup>825</sup>  
755 Realistic simulations of the AGATA Demonstrator+PRISMA spectrome-<sup>826</sup>  
756 ter. *Nuclear Instruments and Methods in Physics Research A*, 622:107–<sup>827</sup>  
757 112, October 2010.
- 758 [17] A. Al-Adili. Simulations of Doppler Effects in Nuclear Reactions for<sup>829</sup>  
759 AGATA Commissioning Experiments. *ArXiv e-prints*, September 2009.
- 760 [18] P. Reiter, B. Bruyneel, J. Eberth, H. Hess, G. Pascovici, N. Warr,<sup>831</sup>  
761 A. Wiens, and H.-G. Thomas. The New Position Sensitive Triple Clus-<sup>832</sup>  
762 ter Detector For AGATA. In J. Jolie, A. Zilges, N. Warr, & A. Blazhev,<sup>833</sup>  
763 editor, *American Institute of Physics Conference Series*, volume 1090 of<sup>834</sup>  
764 *American Institute of Physics Conference Series*, pages 97–101, January<sup>835</sup>  
765 2009.
- 766 [19] L. Nelson, M. R. Dimmock, A. J. Boston, H. C. Boston, J. R. Cresswell,<sup>837</sup>  
767 P. J. Nolan, I. Lazarus, J. Simpson, P. Medina, C. Santos, and C. Parisel.<sup>838</sup>  
768 Characterisation of an AGATA symmetric prototype detector. *Nuclear In-<sup>839</sup>*  
769 *struments and Methods in Physics Research A*, 573:153–156, April 2007.<sup>840</sup>
- 770 [20] H. C. Boston, J. R. Cresswell, M. R. Dimmock, L. Nelson, P. J. Nolan,<sup>841</sup>  
771 S. Rigby, I. Lazarus, J. Simpson, P. Medina, C. Santos, C. Parisel, and<sup>842</sup>  
772 The AGATA Collaboration. Gamma-ray tracking: Characterisation of the<sup>843</sup>  
773 AGATA symmetric prototype detectors. *Nuclear Instruments and Meth-<sup>844</sup>*  
774 *ods in Physics Research B*, 261:1098–1102, August 2007.
- 775 [21] A. J. Boston, M. R. Dimmock, C. Unsworth, H. C. Boston, R. J. Cooper,<sup>846</sup>  
776 A. N. Grint, L. J. Harkness, I. H. Lazarus, M. Jones, P. J. Nolan, D. C.<sup>847</sup>  
777 Oxley, J. Simpson, and M. Slee. Performance of an AGATA asymmetric<sup>848</sup>  
778 detector. In I. Boztosun & A. B. Balantekin, editor, *American Institute of<sup>849</sup>*  
779 *Physics Conference Series*, volume 1072 of *American Institute of Physics<sup>850</sup>*  
780 *Conference Series*, pages 130–135, November 2008.
- 781 [22] C. Unsworth, A. J. Boston, H. C. Boston, S. Colosimo, J. Cresswell, M. R.<sup>852</sup>  
782 Dimmock, F. Filmer, D. Judson, S. Moon, P. J. Nolan, M. J. Norman, and<sup>853</sup>  
783 M. Slee. Characterisation of an asymmetric AGATA detector. In *Soci-<sup>854</sup>*  
784 *ety of Photo-Optical Instrumentation Engineers (SPIE) Conference Se-<sup>855</sup>*  
785 *ries*, volume 7449 of *Society of Photo-Optical Instrumentation Engineers<sup>856</sup>*  
786 *(SPIE) Conference Series*, August 2009.
- 787 [23] M. R. Dimmock, A. J. Boston, J. R. Cresswell, I. Lazarus, P. Medina,<sup>858</sup>  
788 P. Nolan, C. Parisel, C. Santos, J. Simpson, and C. Unsworth. Validation<sup>859</sup>  
789 of Pulse Shape Simulations for an AGATA Prototype Detector. *IEEE<sup>860</sup>*  
790 *Transactions on Nuclear Science*, 56:2415–2425, August 2009.
- 791 [24] M. R. Dimmock, A. J. Boston, H. C. Boston, J. R. Cresswell, L. Nelson,<sup>862</sup>  
792 P. J. Nolan, C. Unsworth, I. H. Lazarus, and J. Simpson. Characterisa-<sup>863</sup>  
793 tion Results From an AGATA Prototype Detector. *IEEE Transactions on<sup>864</sup>*  
794 *Nuclear Science*, 56:1593–1599, June 2009.
- 795 [25] The Agata Collaboration, A. J. Boston, M. R. Dimmock, C. Unsworth,<sup>866</sup>  
796 H. C. Boston, R. J. Cooper, A. N. Grint, L. J. Harkness, I. H. Lazarus,<sup>867</sup>  
797 M. Jones, P. J. Nolan, D. C. Oxley, J. Simpson, M. Slee, and the AGATA<sup>868</sup>  
798 Collaboration. Performance of an AGATA asymmetric detector. *Nuclear<sup>869</sup>*  
799 *Instruments and Methods in Physics Research A*, 604:48–52, June 2009.
- 800 [26] A. J. Boston, M. R. Dimmock, C. Unsworth, H. C. Boston, R. J. Cooper,<sup>871</sup>  
801 A. N. Grint, L. J. Harkness, I. H. Lazarus, M. Jones, P. J. Nolan, D. C.<sup>872</sup>  
802 Oxley, J. Simpson, and M. Slee. Status and Performance of an AGATA<sup>873</sup>  
803 asymmetric detector. In D. Dashdorj, U. Gvaanluvsan, & G. E. Mitchell,<sup>874</sup>  
804 editor, *American Institute of Physics Conference Series*, volume 1109 of<sup>875</sup>  
805 *American Institute of Physics Conference Series*, pages 38–43, March<sup>876</sup>  
806 2009.
- 807 [27] M. Bellato, L. Berti, D. Bortolato, P. J. Coleman-Smith, P. Edelbruck,<sup>878</sup>  
808 X. Grave, R. Isocrate, I. Lazarus, D. Linget, P. Medina, C. Oziol, G. Ram-<sup>879</sup>  
809 pazzo, C. Santos, B. Travers, and A. Triossi. Global Trigger and Readout<sup>880</sup>  
810 System for the AGATA Experiment. *IEEE Transactions on Nuclear Sci-881*
- ence, 55:91–98, 2008.
- [28] F. Zocca, A. Pullia, D. Bazzacco, and G. Pascovici. A Time-Over-  
Threshold Technique for Wide Dynamic Range Gamma-Ray Spec-  
troscopy With the AGATA Detector. *IEEE Transactions on Nuclear Sci-  
ence*, 56:2384–2391, August 2009.
- [29] S. Akkoyun, A. Algora, B. Alikhani, F. Ameil, G. de Angelis, L. Arnold,  
A. Astier, A. Ataç, Y. Aubert, C. Aufranc, and et al. AGATA–Advanced  
Gamma Tracking Array. *Nuclear Instruments and Methods in Physics  
Research A*, 668:26–58, March 2012.
- [30] F. Recchia, D. Bazzacco, E. Farnea, A. Gadea, R. Venturelli, T. Beck,  
P. Bednarczyk, A. Buerger, A. Dewald, M. Dimmock, G. Duchêne,  
J. Eberth, T. Faul, J. Gerl, R. Gernhaeuser, K. Hauschild, A. Holler,  
P. Jones, W. Korten, T. Kröll, R. Krücken, N. Kurz, J. Ljungvall, S. Lu-  
nardi, P. Maierbeck, D. Mengoni, J. Nyberg, L. Nelson, G. Pascovici,  
P. Reiter, H. Schaffner, M. Schlarb, T. Steinhardt, O. Thelen, C. A. Ur,  
J. J. Valiente Dobon, and D. Weißhaar. Position resolution of the pro-  
totype AGATA triple-cluster detector from an in-beam experiment. *Nu-  
clear Instruments and Methods in Physics Research A*, 604:555–562, June  
2009.
- [31] For The Agata Collaboration, F. Recchia, D. Bazzacco, E. Farnea, R. Ven-  
turelli, S. Aydin, G. Suliman, C. A. Ur, and For the AGATA Collab-  
oration. Performance of an AGATA prototype detector estimated by  
Compton-imaging techniques. *Nuclear Instruments and Methods in  
Physics Research A*, 604:60–63, June 2009.
- [32] For The Agata Collaboration, A. Wiens, H. Hess, B. Birkenbach,  
B. Bruyneel, J. Eberth, D. Lersch, G. Pascovici, P. Reiter, H.-G. Thomas,  
and for the AGATA Collaboration. The AGATA triple cluster detector.  
*Nuclear Instruments and Methods in Physics Research A*, 618:223–233,  
June 2010.
- [33] F. Recchia. Installation of the AGATA Demonstrator and commis-  
sioning experiments at LNL. *Journal of Physics Conference Series*,  
205(1):012045–+, January 2010.
- [34] F. Recchia. In-Beam Test of the AGATA Prototype Triple Cluster. *Acta  
Physica Polonica B*, 38:1297–+, April 2007.
- [35] P. A. Söderström, A. Al-Adili, J. Nyberg, F. Recchia, E. Farnea,  
and A. Gadea. Gamma tracking with the AGATA detec-  
tor. In *Proceedings of the 17th International Workshop  
on Vertex detectors. July 28-August 1, 2008. Utö Island,  
Sweden. Published online at ;A href="http://pos.sissa.it/cgi-  
bin/reader/conf.cgi?confid=68";http://pos.sissa.it/cgi-  
bin/reader/conf.cgi?confid=68;A;*, p.40, 2008.
- [36] A. Ataç, A. Kaşkaş, S. Akkoyun, M. Şenyiğit, T. Hüyük, S. O. Kara, and  
J. Nyberg. Discrimination of gamma rays due to inelastic neutron scatter-  
ing in AGATA. *Nuclear Instruments and Methods in Physics Research A*,  
607:554–563, August 2009.
- [37] The Agata Collaboration, M. Doncel, F. Recchia, B. Quintana, A. Gadea,  
E. Farnea, and The AGATA Collaboration. Experimental test of the  
background rejection, through imaging capability, of a highly segmented  
AGATA germanium detector. *Nuclear Instruments and Methods in  
Physics Research A*, 622:614–618, October 2010.
- [38] M. Doncel, F. Recchia, A. Gadea, E. Farnea, and B. Quintana. Compton  
Imaging Capabilities of AGATA for Background Rejection. In J. A. Cab-  
ballero, C. E. Alonso, M. V. Andrés, J. E. García Ramos, & F. Pérez-  
Bernal, editor, *American Institute of Physics Conference Series*, volume  
1231 of *American Institute of Physics Conference Series*, pages 213–214,  
April 2010.
- [39] J. Gerl. Nuclear Spectroscopy Studies at GSI – from Rising to HIS-  
PEC/DESPEC. *Acta Physica Polonica B*, 40:767–+, March 2009.
- [40] M. Winkler, H. Geissel, H. Weick, B. Achenbach, K.-H. Behr,  
D. Boutin, A. Brünle, M. Gleim, W. Hüller, C. Karagiannis, A. Kelic,  
B. Kindler, E. Kozlova, H. Leibrock, B. Lommel, G. Moritz, C. Mühle,  
G. Münzenberg, C. Nociforo, W. Plass, C. Scheidenberger, H. Simon,  
K. Sümmerer, N. A. Tahir, A. Tauschwitz, M. Tomut, J. S. Winfield, and  
M. Yavor. The status of the Super-FRS in-flight facility at FAIR. *Nu-  
clear Instruments and Methods in Physics Research B*, 266:4183–4187,  
October 2008.
- [41] P. Bednarczyk, J. Grębosz, M. Kmiecik, A. Maj, W. Męczyński, J. Sty-  
czeń, C. Domingo-Pardo, P. Doornenbal, Gerl J., M. Górńska, H. J. Woller-  
sheim, J. Jolie, P. Reiter, A. Bracco, and F. Camera. In-beam  $\gamma$ -ray angu-  
lar distribution and lifetime measurements - experience from rising and  
perspectives at FAIR. *Acta Physica Polonica B*, 41:505–+, January 2010.

- 882 [42] H. Geissel, P. Armbruster, K. H. Behr, A. Brünle, K. Burkard, M. Chen,  
883 H. Folger, B. Franczak, H. Keller, O. Klepper, B. Langenbeck, F. Nickel,  
884 E. Pfeng, M. Pfützner, E. Roeckl, K. Rykaczewski, I. Schall, D. Schardt,  
885 C. Scheidenberger, K.-H. Schmidt, A. Schröter, T. Schwab, K. Sümmerer,  
886 M. Weber, G. Münzenberg, T. Brohm, H.-G. Clerc, M. Fauerbach, J.-J.  
887 Gaimard, A. Grewe, E. Hanelt, B. Knödler, M. Steiner, B. Voss, J. Weck-  
888 enmann, C. Ziegler, A. Magel, H. Wollnik, J. P. Dufour, Y. Fujita, D. J.  
889 Vieira, and B. Sherrill. The GSI projectile fragment separator (FRS): a  
890 versatile magnetic system for relativistic heavy ions. *Nuclear Instruments*  
891 *and Methods in Physics Research B*, 70:286–297, August 1992.
- 892 [43] D. Rudolph et al. LYCCA - the Lund York Cologne CAlorimeter. Tech-  
893 nical report, FAIR TAC HISPEC/DESPEC, 2010.
- 894 [44] H. J. Wollersheim, D. E. Appelbe, A. Banu, R. Bassini, T. Beck,  
895 F. Becker, P. Bednarczyk, K.-H. Behr, M. A. Bentley, G. Benzoni,  
896 C. Boiano, U. Bonnes, A. Bracco, S. Brambilla, A. Brunle, A. Burger,  
897 K. Burkard, P. A. Butler, F. Camera, D. Curien, J. Devin, P. Doornenbal,  
898 C. Fahlander, K. Fayz, H. Geissel, J. Gerl, M. Gorska, H. Grawe, J. Gre-  
899 bosz, R. Griffiths, G. Hammond, M. Hellstrom, J. Hoffmann, H. Hubel,  
900 J. Jolie, J. V. Kalben, M. Kmiecik, I. Kojouharov, R. Kulesa, N. Kurz,  
901 I. Lazarus, J. Li, J. Leske, R. Lozeva, A. Maj, S. Mandal, W. Meczyn-  
902 ski, B. Million, G. Munzenberg, S. Muralithar, M. Mutterer, P. J. Nolan,  
903 G. Neyens, J. Nyberg, W. Prokopowicz, V. F. E. Pucknell, P. Reiter,  
904 D. Rudolph, N. Saito, T. R. Saito, D. Seddon, H. Schaffner, J. Simpson,  
905 K.-H. Speidel, J. Styczen, K. Summerer, N. Warr, H. Weick, C. Wheldon,  
906 O. Wieland, M. Winkler, and M. Zieblinski. Rare ISotopes INvestigation  
907 at GSI (RISING) using gamma-ray spectroscopy at relativistic energies.  
908 *Nuclear Instruments and Methods in Physics Research A*, 537:637–657,  
909 February 2005.
- 910 [45] D. Bazzacco. mgt code developed within the tmr program 'gamma-ray  
911 tracking detectors'.
- 912 [46] C. Nochiforo, private communication.
- 913 [47] J. A. Grau, Z. W. Grabowski, F. A. Rickey, P. C. Simms, and R. M.  
914 Steffen. Measurements of Directional Correlation from Oriented Nuclei  
915 (DCO) and the Band Structure in  $^{102}\text{Pd}$ . *Physical Review Letters*, 32:677–  
916 680, March 1974.
- 917 [48] P. Bednarczyk, J. Grębosz, A. Maj, M. Kmiecik, W. Męczyński, J. Sty-  
918 czeń, H. J. Wollersheim, J. Gerl, M. Górska, P. Reiter, A. Bracco, and  
919 F. Camera. Gamma-Ray Angular Distribution in Coulomb Excitation  
920 Experiments at Intermediate Energies as a Signature of Electromagnetic  
921 and Nuclear Forces in Peripheral Collisions. *Acta Physica Polonica B*,  
922 40:853–+, March 2009.
- 923 [49] T. R. Saito, N. Saito, K. Starosta, J. Beller, N. Pietralla, H. J. Wollersheim,  
924 D. L. Balabanski, A. Banu, R. A. Bark, T. Beck, F. Becker, P. Bednarczyk,  
925 K.-H. Behr, G. Benzoni, P. G. Bizzeti, C. Boiano, A. Bracco, S. Bram-  
926 billa, A. Brünle, A. Bürger, L. Caceres, F. Camera, F. C. L. Crespi,  
927 P. Doornenbal, A. B. Garnsworthy, H. Geissel, J. Gerl, M. Górska, J. Gre-  
928 bosz, G. Hagemann, J. Jolie, M. Kavatsyuk, O. Kavatsyuk, T. Koike,  
929 I. Kojouharov, N. Kurz, J. Leske, G. Lo Bianco, A. Maj, S. Mallion,  
930 S. Mandal, M. Maliage, T. Otsuka, C. M. Petrache, Z. Podolyak,  
931 W. Prokopowicz, G. Rainovski, P. Reiter, A. Richard, H. Schaffner,  
932 S. Schielke, G. Sletten, N. J. Thompson, D. Tonev, J. Walker, N. Warr,  
933 O. Wieland, and Q. Zhong. Yrast and non-yrast  $2^+$  states of  $^{134}\text{Ce}$  and  
934  $^{136}\text{Nd}$  populated in relativistic Coulomb excitation. *Physics Letters B*,  
935 669:19–23, October 2008.
- 936 [50] P. Detistov, D. L. Balabanski, and Z. Podolyak. Simulation of the Elec-  
937 tromagnetic Background Radiation for the Rising Experimental Set-Up.  
938 *Acta Physica Polonica B*, 38:1287–+, April 2007.
- 939 [51] P. Doornenbal, P. Reiter, H. Grawe, T. Saito, A. Al-Khatib, A. Banu,  
940 T. Beck, F. Becker, P. Bednarczyk, G. Benzoni, A. Bracco, A. Bürger,  
941 L. Caceres, F. Camera, S. Chmel, F. C. L. Crespi, H. Geissel, J. Gerl,  
942 M. Górska, J. Grębosz, H. Hübel, M. Kavatsyuk, O. Kavatsyuk,  
943 M. Kmiecik, I. Kojouharov, N. Kurz, R. Lozeva, A. Maj, S. Man-  
944 dal, W. Meczynski, B. Million, Z. Podolyak, A. Richard, N. Saito,  
945 H. Schaffner, M. Seidlitz, T. Striepling, J. Walker, N. Warr, H. Weick,  
946 O. Wieland, M. Winkler, and H. J. Wollersheim. Lifetime effects for high-  
947 resolution gamma-ray spectroscopy at relativistic energies and their im-  
948 plications for the RISING spectrometer. *Nuclear Instruments and Meth-*  
949 *ods in Physics Research A*, 613:218–225, February 2010.